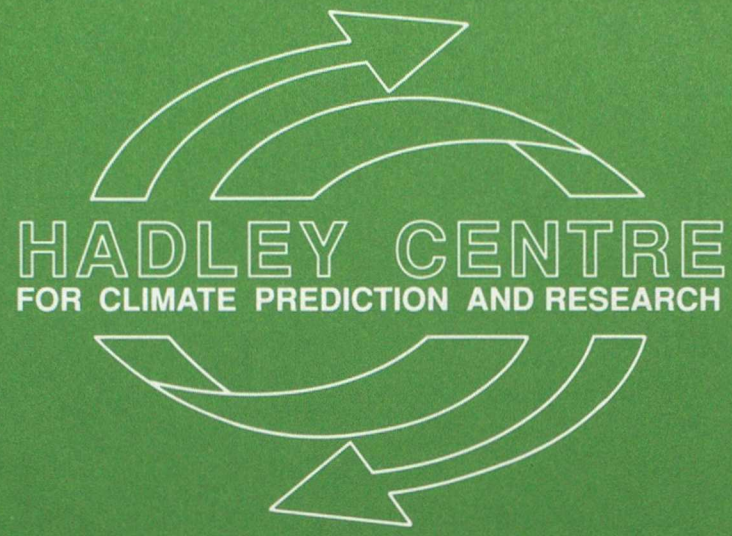

Simulation of the tropical Pacific using a simplified ocean model

by

M A Balmaseda, D L T Anderson and M K Davey

CRTN 49

June 1994

CLIMATE
RESEARCH
TECHNICAL
NOTE

Hadley Centre
Meteorological Office
London Road
Bracknell
Berkshire RG12 2SY

CLIMATE RESEARCH TECHNICAL NOTE NO. 49

SIMULATION OF THE TROPICAL PACIFIC USING A SIMPLIFIED OCEAN MODEL

by

M.A. Balmaseda, D.L.T. Anderson, M.K. Davey

Hadley Centre for Climate Research and Prediction
Meteorological Office
London Road
Bracknell
Berkshire RG12 2SY
U.K.

Note: This paper has not been published. Permission to quote from it should be obtained from the Director of the Hadley Centre

Simulation of the Tropical Pacific using a simplified ocean model

Magdalena A. Balmaseda *, David L.T. Anderson*, Michael K. Davey**

*: Atmospheric, Oceanic and Planetary Physics, Clarendon Laboratory,
University of Oxford, Parks Road, Oxford, OX1 3PU, England

**: Hadley Centre, Meteorological Office,
London Road, Bracknell, Berkshire RG12 2SZ, England

Abstract

This paper presents the results of a 33 year integration of a simplified ocean model of the tropical Pacific. The model is forced with observed winds provided by the Florida State University, for the period 1961 to 1993. The analysis of sea surface temperature and heat content gives insight into the mechanism controlling the thermodynamics of the ocean and the role of remote/local forcing.

The model reproduces the interannual variability of sea surface temperature anomalies in regions of the central equatorial Pacific rather well, but there are notable discrepancies between model and observations near the South American coast, which probably are a result of the model parameterization of the upwelling. The warmings in the central and eastern Pacific are caused by Kelvin waves excited by the winds in the west, via depression of the thermocline and suppression of climatological upwelling. In the regions farther west, the cause of the warming is related to horizontal advection.

The relationship between the model heat content anomalies and the wind field is consistent with that maintained between the observed sea level and wind stress. The evolution of heat content anomalies suggests the presence of an inter-hemispheric exchange of energy associated with the ENSO cycle. The cyclic structure of the heat content is described in detail: the heat content in the equatorial western Pacific increases during the cold phase of ENSO, with a subsequent loss of this heat toward higher latitudes during the warm phases. The role of Rossby and Kelvin waves in this cycle is analyzed. It appears that Kelvin waves resulting from the reflection of Rossby waves off the western boundary are confined to the western Pacific, contributing to the accumulation of heat there: they do not have a major influence on the heat content in the central Pacific. Rather, the anomalies of heat content in the central Pacific are determined by local winds, or by winds in regions just to the west.

1. Introduction

Two decades ago, Bjerknes (1966, 1969) established the basis of our present understanding of the ENSO (El Niño / Southern Oscillation). His thesis was that El Niño and the Southern Oscillation were related, and that the interaction between the ocean and the atmosphere was the key for both phenomena. In his scenario, warmings in the Eastern Pacific were caused by the weakening of the equatorial Trade Winds, leading to a reduction in equatorial upwelling.

Although reduction in locally forced upwelling can be an important component in oceanic warmings, attention has been focused on remote processes invoking ocean waves and advection. A weakening of the zonal wind in the Western and central Pacific would generate Kelvin wave packets, which would propagate eastward and depress the thermocline in the eastern Pacific. As this is a region of vigorous upwelling, a reduction in upwelling of colder water (produced by a depressed thermocline) would soon cause a positive sea surface temperature (SST) anomaly there. At the same time, Rossby waves are also excited which may later act to reduce this effect. The first coupled models to invoke Kelvin and Rossby waves in a comprehensive way were those of McCreary (1983), McCreary and Anderson (1985), and Schopf and Suarez (1988). However, neither of these effects would explain SST changes in the oceanic regions where there is either no upwelling, or where upwelling is very weak. One could expect the contribution of horizontal advection and surface heat flux to be important. Gill (1983) and Schopf and Harrison (1983) suggest that anomalies in horizontal advection play an important role in the development of El Niño events.

Later studies with ocean-atmosphere coupled models (Hirst 1986, Wakata and Sarachik 1991, Giese and Harrison 1990, Neelin 1990) show that the ocean thermodynamics determines the nature of oscillations in the coupled system: in those models in which the evolution of SST depends on the thermocline depth, the instability has its origin in the Western Pacific, and propagates eastward as a coupled Kelvin mode (Anderson and McCreary 1985, Yamagata and Masumoto 1989, Philander 1984). In models where the SST anomaly is determined by horizontal advection, the unstable modes are Rossby modes, that propagate westward (Rennick and Haney, 1986). When the two mechanisms compete, the instability can be stationary (Zebiak and Cane (1987), Schopf and Suarez (1988), Battisti and Hirst (1989), Xie et al. (1989)). Many of these aspects of ENSO have been reviewed by McCreary and Anderson (1991) and Neelin *et al* (1994).

A deeper knowledge of the behaviour of the ocean is necessary in order to better

understand the nature of ENSO. A direct analysis of observations is not easy because of the sparsity of data. An alternative procedure is to analyze the output of an ocean model when forced by real winds. This could allow the quantitative study of the heat budget of the ocean, as well as the diagnosis of the structure of the different variables before and during the events. In this approach, several ocean models of different complexity have been forced with observed winds (Busalacchi and O'Brien 1980, Busalacchi *et al* 1983, Philander and Siegel 1985, Cane 1984, Zebiak and Cane 1987, Seager 1989). Intercomparison of different models can help us to understand how the results depend upon the model or the forcing fields (Miller *et al* 1993).

The present work is an attempt to simulate the evolution of the sea surface temperature during the period 1961-1993, with attention focused on the features of its interannual variability. To do that, an ocean model of intermediate complexity (2 and 1/2 layers) is forced with the observed wind stresses from Florida State University (Goldenberg and O'Brien 1981), for 33 years (1961-1993). From an analysis of the results the mechanisms responsible for the changes in SST at interannual time scales can be identified. To determine the relative importance between remote and local forcing, and to clarify the role of oceanic waves in the evolution of SST, attention has been focussed on the upper ocean heat content and its correlation with the winds.

In section 2, we describe the ocean model and the procedure used to analyze the results. Section 3 contains a discussion of the evolution of the modelled SST including, where possible, comparison with observations and analysis of the contribution of the different flux processes in the heat budget. The interannual variability of the model heat content and its relation with the wind field is addressed in section 4. In section 5, a description of the ENSO cycle simulated by the model is provided, based on the information yielded by a Principal Oscillation Pattern (POP) analysis. Finally, some conclusions are given in section 6.

2. Model formulation and analysis methods

2.1. Model formulation

The ocean model is one of intermediate complexity, derived from that described in Anderson & McCreary (1985), but extended to two active layers. It consists of depth-averaged primitive equations in two active layers, overlying a deep inert layer. The model allows for an exchange of mass between layers by means of a parameterization of entrainment. Consequently, vertical fluxes of heat and momentum are permitted.

The model includes explicit nonlinear thermodynamics for both layers, accounting for horizontal advection, vertical heat transport, diffusion and, in the first layer, surface heat flux. The heat flux consists of the seasonal heat flux estimated by Oberhuber (1988) plus a relaxation term to a prescribed climatology. The strength of the relaxation is given by a local factor λ, also provided by Oberhuber. This can vary from place to place but typically has an amplitude of 35 $W/m^2/K$. The equatorial β-plane is adopted, so that $f = \beta y$. The model equations are:

$$(\frac{\partial}{\partial t} + \frac{\partial}{\partial x}u_i + \frac{\partial}{\partial y}v_i + \underline{f}\wedge)h_i\underline{v}_i = \frac{-h_i}{\rho_0}\nabla p_i + \underline{\mathcal{M}}_i(\mathcal{E}) + \frac{\underline{\tau}}{\rho_0} + \nu\nabla^2 h_i\underline{v}_i \tag{1}$$

$$(\frac{\partial}{\partial t} + \frac{\partial}{\partial x}u_i + \frac{\partial}{\partial y}v_i)h_i = -(-1)^i\mathcal{E} + \zeta\nabla^2 h_i \tag{2}$$

$$(\frac{\partial}{\partial t} + u_i\frac{\partial}{\partial x} + v_i\frac{\partial}{\partial y})T_i = Q_s + \mathcal{H}_i(\mathcal{E}) + \kappa\nabla^2 T_i \tag{3}$$

Here $i = 1, 2$ is the layer index, $\underline{v} = (u_i, v_i)$ is (zonal, meridional) horizontal velocity, p_i is pressure, h_i is layer depth, T_i is temperature, $\mathcal{E}$ is the entrainment, Q_s is the surface heat flux, $\underline{\mathcal{M}}$ and $\mathcal{H}$ are the vertical advection terms of momentum and heat respectively, and $\underline{\tau} = (\tau_x, \tau_y)$ is the wind stress. Both surface heat flux and wind stress act only on the first layer. Below layer 2, the ocean is at rest with a constant temperature $T_3 = 5°\mathrm{C}$.

The pressure gradients are averaged in depth, and have the following expressions:

$$\frac{1}{\rho_0}\nabla p_1 = g\alpha\nabla(h_1(T_1 - T_3) + h_2(T_2 - T_3)) - g\alpha h_1\nabla T_1/2 \tag{4}$$

$$\frac{1}{\rho_0}\nabla p_2 = g\alpha(T_2 - T_3)\nabla(h_1 + h_2) - g\alpha(h_2/2 + h_1)\nabla T_2 \tag{5}$$

where g is the acceleration of gravity, α is the coefficient of thermal expansion (assumed constant), and T_3 is the constant temperature of the third layer.

The entrainment velocity $\mathcal{E}$ is determined by limits on the depth of the upper layer, and is a modification of the parameterization used by McCreary and Kundu (1988):

$$\mathcal{E} = \begin{cases} (H_e - h_1)^2/t_e H_e & \text{if } h_1 \le H_e \\ -(H_d - h_1)^2/t_d H_d & \text{if } h_1 \ge H_d \end{cases} \tag{6}$$

As well as the exchange of mass between layers, there is corresponding exchange of heat and momentum:

$$\underline{\mathcal{M}}_i(\mathcal{E}) = \begin{cases} -(-1)^i \mathcal{E} \underline{v}_2 & \text{if } \mathcal{E} \geq 0 \text{ (upwelling)} \\ -(-1)^i \mathcal{E} \underline{v}_1 & \text{if } \mathcal{E} \leq 0 \text{ (downwelling)} \end{cases} \tag{7a}$$

$$\mathcal{H}_1(\mathcal{E}) = \begin{cases} -\mathcal{E}\gamma(T_1 - T_2)/h_1 & \text{if } \mathcal{E} \geq 0 \\ 0 & \text{if } \mathcal{E} \leq 0 \end{cases} \tag{7b}$$

$$\mathcal{H}_2(\mathcal{E}) = \begin{cases} 0 & \text{if } \mathcal{E} \geq 0 \\ -\mathcal{E}(T_1 - T_2)/h_2 & \text{if } \mathcal{E} \leq 0 \end{cases} \tag{7c}$$

Here γ is a parameter controlling the effective vertical temperature gradient. The values of the constants are shown in Table 1.

The model uses a C grid layout, with a resolution of 1.5 $\times$ 1.5 degrees (latitude-longitude), covering an extension from 30°S - 30°N in latitude and from 123°E - 69°W in longitude. The time step for integration is two hours. The boundaries are closed, with free slip conditions.

2.2. The modelling strategy

The ability of the ocean model to reproduce the interannual variability of SST has been tested by forcing the ocean model with observed FSU winds during the period 1961-1993, which have been detrended by a procedure based on Singular Spectral Analysis, that effectively uses a filter with a 10-year window (Allen 1992). The wind stress used to force the model was computed from the detrended pseudostress as:

$$\underline{\tau} = \mu \rho_a C_a \mid \underline{\mathbf{U}} \mid \underline{\mathbf{U}} \tag{8}$$

where $\underline{\mathbf{U}}$ is the wind speed (m/s), $\rho_a = 1.2 Kgm^{-3}$ is the density of air, C_a is the drag coefficient, taken to have the value $C_a = 0.0015$, and μ is a parameter controlling the strength of the forcing.

The model was first spun up for 10 years with climatological wind stress and heat flux Q_s as forcing fields. The climatological wind stress used consisted of the seasonal mean of the FSU stress and the heat flux was represented by the Oberhuber heat flux plus a relaxation term to T_0 , the observed SST:

$$Q_s = Q_0 + \lambda(T - T_0) \tag{9a}$$

Here T is the model SST, Q_0 and T_0 are monthly climatological heat flux and SST, and λ (which is negative) controls the rate of relaxation to the observed SST. Climatological values are taken from Oberhuber (1988). Initial values were $h_1 = 100m$, $h_2 = 175m$, $T_2 = 16°\mathrm{C}$, and $T_1 = 22 + 8\cos^2(\pi y/30)$ at latitude y degrees.

Once we obtained the model climatology, we began the 33 years run, forcing the model with the detrended FSU wind stress, from January 1961 to December 1993. The initial state was taken to be December of the model seasonal cycle. For this extended integration (control run) the surface heat formulation was modified to

$$Q_s = Q_0 + \lambda(T_m - T_0) + 0.2\lambda(T - T_m) \qquad (9b)$$

where T_m represents the model SST climatology. The factor 0.2 allows a weaker relaxation to the model seasonal cycle, so that the model SST anomalies have similar magnitude to those observed (Stockdale, 1992).

2.3 Analysis procedure

The values of the variables at day 15 of each month are taken to represent the monthly values. The monthly anomalies are departures from the monthly mean of the model results over the period 1966-1985.

Comparison between model results and observations is possible in the case of SST; the observed SST are provided by the COADS (Comprehensive Oceanic and Atmospheric Data Set) from 1961 to 1986 and the CAC (Climatic Analysis Center) data set thereafter (Reynolds, 1988 and Reynolds and Marsico, 1993) from 1982 to 1993. Both datasets have been linearly merged during the period 1982-1986. The dominant modes of model SST variability are provided by an EOF (Empirical Orthogonal Function) analysis of this field. To explore the contribution of the different terms in the heat budget, and to allow a comparison with results of other models discussed by Miller *et al* (1993) (M93 in what follows), a linear regression between the dominant modes of model SST and the time series of the different advection terms is carried out. The result of this analysis will be a set of patterns, called Associated Patterns (AP), that represent the spatial distribution of the advection variability which is linearly related to the variability of the SST anomalies.

To determine the relative importance between remote and local forcing, and, in this way, to clarify the role of large scale oceanic waves in the evolution of the SST, we will focus our attention on the anomalies of heat content of the upper ocean, which are

defined to be proportional to fluctuations of sea level:

$$HC = \frac{(T_1 - T_3)h_1 + (T_2 - T_3)h_2}{H_1 + H_2} \tag{10}$$

To allow an easier comparison and correlation analysis, the ocean domain is divided into several standard regions Niño1-4 and Eq1-3 (see table 2 and figure 1). The anomalies will be averaged over these regions.

In order to get qualitative information about the dominant spatial and propagating features of the variables, a Principal Oscillation Pattern (POP) analysis (Hasselmann 1988) has been carried out on the fields SST, HC and the zonal component τ_x of surface wind stress. The POP technique combines the spectral information provided by ARMA (Auto-Regressive Moving Average) methods with the spatial information provided by the covariance matrix, and it is useful in extracting oscillatory features of the analyzed fields. The technique, outlined below, has been extensively used for analysis and prediction of the variability of climatic data fields (Xu and von Storch 1990, Blumenthal 1991, Latif *et al* 1993, Wu *et al* 1994, Balmaseda *et al* 1994).

Given a data field $X(t,q)$ (where t is the time index for variable q), the POP technique assumes that it can be represented by a first-order autoregressive multivariate process. Under this hypothesis, a system matrix B can be computed by a least square procedure. Blumenthal (1991) argues that this method constitutes an empirical linearization of a non-linear system, so that the system can be represented by:

$$X(t + \Delta t, k) = B_{k,l} X(t, l) \tag{11}$$

The diagonalization of matrix B provides the modal decomposition of the system. Any complex eigenvalues ($\lambda = \mu + i\nu$) will be associated with oscillatory modes of period $T = 2\pi / \arctan(\nu/\mu)$ and e-folding time $e = -1/\ln(\mid \lambda \mid)$. Real eigenvalues are associated with purely damped modes.

The evolution of the system is easier to understand using the basis set of eigenvectors of B, whereby each mode is decoupled from the others. In this basis, each mode evolves as:

$$Z(t + \Delta t, l) = \lambda_l Z(t, l), \; l = 1, ..., q \tag{12}$$

In equation 12, the $Z(t,l)$ are called the coefficients of the lth POP mode. For an oscillatory mode, these coefficients are complex, and are uniquely determined except for phase and normalization. The phase will be chosen here such that the real part of the coefficients represents the *peak* phase of ENSO and the imaginary coefficients the *transition* phase. This can be achieved if the real coefficients exhibit the largest correlation with the observed SST anomalies in Niño3 (or other conventional index of ENSO) at lag zero. Therefore, a transformation is carried out for each POP pair such that the real coefficients are maximally correlated with Niño3 index.

3. Model results: Sea Surface Temperatures

3.1. General Features

Differences between the model SST seasonal cycle and observed climatology can be seen in figure 2 for the four months March, June, September and December. The model is warmer than observations in the western equatorial Pacific throughout the year. In the eastern part of the equatorial ocean, the errors are more seasonally dependent. The largest differences occur in spring (figure 2a), when the model is up to 2 degrees colder than observations in the eastern Pacific. The model also fails to reproduce the effects of coastal upwelling along the South American coast, and so the model SST is too high compared with observations (except in March). These errors could result from errors in the wind or from deficiencies in the model. However, they are not specific to our model but occur in many other models also, despite strong forcing to the seasonal cycle of SST (Stockdale *et al.* 1993). The cause of the error is not clear, but may result in part from the fact that we have used monthly wind stresses, which do not represent the high frequency variability. The model seasonal cycle in the extra equatorial latitudes is weaker than observed, with model SST less warm in summer and less cold in winter than observations.

The time-longitude diagram of the model equatorial SST anomalies is shown in figure 3a, while the observed SST are shown in figure 3b. In general, the model reproduces the observed sequence of warm and cold events quite well. However, the generation and evolution of the model anomalies differ from observations in some aspects. In the model, disturbances originate in the east/central regions EQ1 and EQ2, and then propagate both eastward and westward, in contrast to the observed SST, for which propagating features are less clear and vary from event to event. In the model, the eastward propagation of the anomalies is inhibited: only in strong El Niño events (1972-73, 1982-83, 1992-93) do warm anomalies approach the eastern boundary. The model produces a

spurious warming at the beginning of 1984 and at the end of 1985 in the eastern part of the ocean, and strong cold anomalies in the central part. These effects seem to be the response of the model to the westerly winds in the eastern Pacific. It is interesting to note that the same spurious warming occurs in the experiment by Seager (1989), when he forced his ocean model with the same set of winds (not detrended). In his paper, Seager argues that this error in his model results from deficiencies in surface heat flux parameterization (because in his model the wind speed is the main source of variability in the surface heat flux). This is not the case in our model, in which the surface heat flux does not depend directly on the wind. Whether the failure is due to the incorrect response of the model to the wind forcing, or to errors in the wind field, is something that has not been determined, although, as will be discussed later in this section, several models produce similar results when forced with the same winds.

In order to quantify the performance of the model over the whole model domain, a point to point comparison between model and observations has been carried out. Statistical scores such as correlation, hindcast skill and root mean square error (RMS) have been computed for each point of the model grid. For this purpose, observations from COADS have been interpolated to the model domain, and the time series have been smoothed by a 5-month running mean filter. This filter will allow more direct comparison with the results presented by M93. Figures 4a-c shows the spatial distribution of the point to point statistics.

The RMS error, defined as $\epsilon = \langle (T_m - T_0)^2 \rangle^{1/2}$, represents the time averaged <> error between observed anomalies T_0 and model anomalies T_m. As shown in figure 4a, the largest RMS error is located in the eastern Pacific, along the coast of South America, where it reaches values over 1°C. This error is an indication of the lack of variability of model SST in this region. In the remainder of the basin, the RMS error is much smaller, with typical values of $0.4 - 0.6$°C. The pattern of the RMS of the present model is different to the RMS pattern of the general circulation (GCM) and simple models discussed in M93. It shares with the GCMs the high values of RMS near the South American coast, where the wave dynamics and mixing processes are poorly represented. In the western Pacific however, the RMS errors are small in contrast to the GCMs, which tend to overestimate the size of the SST anomalies in this area, so producing large values of the RMS error.

Although the RMS error is lower in the western Pacific, the explained variance is poor in this region. Figure 4b represents the quantity *hindcast skill*, which is defined as $S = 1 - \epsilon^2 / \langle (T_0)^2 \rangle$, and constitutes a measure of the observed variance explained by the model simulation. ($S = 1$ if $T_m = T_o$, and $S < 0$ when the RMS error exceeds the

observed standard deviation.) The model exhibits a peak in skill in the central Pacific, with values between 0.4 and 0.5. The shape of the skill pattern of the model resembles the skill pattern of the Latif MPIZ GCM (see M93) with a skill peak in the central Pacific on both sides of the equator, while in the eastern Pacific the maximum of the skill occurs just over the Equator. In the western Pacific, the skill is negative, indicating that the model has poorer performance in this region.

As a measure of the phase of observed and model SST variations, the anomaly correlation between model and observation ($r = \langle T_0 T_m \rangle / (\langle (T_0)^2 \rangle \langle (T_m)^2 \rangle)^{1/2}$) has been plotted in figure 4c. The correlation values are generally larger than the skill values, but with a very similar pattern. The maximum (0.7-0.8) is achieved over a relatively broad area in the central Pacific, decreasing smoothly westward and eastward. There are also patches of high correlation between model and observations in the central-west Pacific, near 20°N and 25°S.

The resemblance of the patterns of skill and anomaly correlation between the present model and the MPIZ model (as shown in M93) is remarkable, even when the first is an intermediate ocean layer model and the second is a GCM. The similarity (concerning both extension and shape) may be attributed to the similar influence that the zonal advection has in both models. The patterns are not so similar in the case of the Lamont simplified ocean model, even though it is a model of comparable complexity to the present one. The reason for that may lie in the different representation of the horizontal advection terms by each of the models in the central Pacific, and mixing processes in the eastern Pacific.

3.2. Causes of SST variations

In order to identify the large scale relationship between the SST anomalies and the mechanisms causing their variations, a linear regression has been performed between the dominant modes of model SST and the anomalies of different upper layer advection terms

$$ADVU = -u_1 \partial T_1 / \partial x \ , \quad ADVV = -v_1 \partial T_1 / \partial y \ , \quad ADVW = \mathcal{H}_1(\mathcal{E})$$

(zonal, meridional and vertical respectively: see equation 3).

The expression for the vertical advection term is given in equation 7b. The sign of the advection terms have been chosen such that positive values mean a tendency to increase SST. The advection anomalies have been computed with respect to the monthly average climatology. For example, a positive anomaly in $ADVW$ corresponds to an anomalous SST warming tendency due to a decrease in cooling by upwelling.

The dominant modes of variability of the SST have been selected via an EOF analysis. Figures 5a-c show the spatial patterns of the first 3 dominant modes resulting from the EOF analysis of the model SST anomalies. The corresponding Principal Components (PCs, sometimes also called the associated timeseries) are given in figure 6. During the major events, there is a persistent phase difference between the first and the third PCs, with the first PC leading the third by about 9 months. The second PC exhibits very little variability, except during the large event of 1982/1983 when there is a large peak lagging the peak of the first PC. This peak, together with the spatial pattern, accounts for the eastward propagation of the SST during this episode. The second PC exhibits markedly different behaviour during the '70s and during the '80s, with noticeably smaller amplitude during the '70s. Whether this "decadal" variability is also present in observations needs to be investigated.

The first three PCs have been used to compute the Associated Patterns (AP) of each of the anomalous advection terms, as follows:

$$APU_k(x,y) = \sum_{t=1}^{t=n} ADVU'(x,y,t)\ PC_k(t) \qquad (13a)$$

$$APV_k(x,y) = \sum_{t=1}^{t=n} ADVV'(x,y,t)\ PC_k(t) \qquad (13b)$$

$$APW_k(x,y) = \sum_{t=1}^{t=n} ADVW'(x,y,t)\ PC_k(t) \qquad (13c)$$

where $'$ denotes perturbations from monthly average climatology. Thus APU_1 is the zonal advection pattern that usually appears when SST EOF1 appears, etc. Where the AP and EOF patterns have the same *sign* the AP acts to reinforce the SST anomaly, and conversely opposite sign signifies damping.

The first SST mode (figure 5a) accounts for 59.2% of the variability. The strongest signal is in the central eastern Pacific, around 130°W, and seems to be symmetric about the Equator. The latitudinal extension is largest in the region of the maximum at 130°W, decreasing eastward (in contrast to the first observed EOF, which has its greatest latitudinal extent in the east), and EOF 1 has the same sign over almost the whole basin. Figures 7a, b and c show the patterns APW_1, APU_1 and APV_1 associated with the first EOF of model SST. Strong changes in vertical advection in the eastern Pacific seem to be responsible for the SST anomalies in the eastern Pacific. APW_1 is positive in a narrow band centred on the equator, with a maximum located around 110°W. (Here $APW > 0$ where EOF 1 is positive, indicating that warm SST anomalies

are supported by decreased upwelling.) In the regions east of 130°W, the reinforcing effect of APW_1 clearly dominates the damping contribution of the zonal advection. In regions west of 130°W APW_1 is almost zero: the SST variations here associated with the first EOF mode are produced by zonal advection, which seems to determine the extent of the SST anomaly. The contribution of meridional advection (APV_1) is small, and only affects the eastern part of the basin. This upwelling and zonal advection behaviour of the first mode of SST is similar to that of the first mode found by M93 for the MPIZ model. However, meridional advection contributes much more strongly in MPIZ, particularly in the central part of the ocean: this may determine the shift towards the west of the maximum of the SST anomaly in the MPIZ model.

The second EOF mode of SST (figure 5b) has a nodal line around 130°W with positive sign to the east and negative to the west. As we mentioned above, this mode is weak in the evolution of SST, except during the large event in 1982-1983. Even so, the mode accounts for 13% of the total variance. A distinct feature of this pattern is a well pronounced and broad maximum of SST along the American coast. The associated patterns are given in figure 8. The AP patterns are largest near the equatorial nodal point for EOF2, where APU is positive, APW negative, and APV relatively small. The main contribution to the second mode is the zonal advection term. The vertical advection has a secondary role this time, reinforcing EOF2 west of the node line and damping it to the east.

Apart from the 1982/1983 case, the SST evolution seems to be characterized by the alternance of EOF 1 and EOF 3, which would result in almost stationary evolution in the central/east Pacific. The third EOF mode of SST is shown in figure 5c, and the associated patterns of the advection terms appear in figures 9a-c. The third SST mode accounts for 10% of the total variance, and appears as a narrow peak centred on the Equator near 125°W. Both the longitudinal and latititudinal extensions of this peak are smaller than in the first EOF: to the west, the anomalies change sign at about 160°W, and they do not reach the eastern coast. The anomalies also change sign at 5 degrees off the equator, and secondary maxima of opposite sign appear at about 10 degrees. This pattern of SST is reminiscent of waves in the central Pacific. The mechanisms exciting this mode are very similar to those exciting the first mode. The vertical advection acts over a larger area of the eastern and central Pacific, with a maximum at 120°W (slightly to the west of the maximum of vertical advection in the first mode). The zonal advection also has a damping effect in the eastern basin, which seems to be more effective than the damping effect in the first mode, inhibiting the SST anomalies approaching the coast. However, west of 120°W, zonal advection reinforces the vertical advection in generating

SST anomalies. It does not have any influence beyond the dateline though, and the SST anomalies do not penetrate farther west. Meridional advection only acts in the eastern Pacific, and its contribution has the same sign as the vertical advection.

In summary, from the point of view of the mechanisms causing the variation of model SST anomalies, the equatorial Pacific could be divided in three distinct regions: in region EQ1, in the eastern Pacific between 130°W and 90°W, the SST evolution seems to be dominated by the vertical advection term; the effects of the vertical advection are enhanced by the contribution of the meridional advection and damped by the zonal advection. Only during the 82/83 warm episode does the zonal advection contribution dominate the contribution of vertical and meridional terms, causing eastward propagation of the SST anomalies. Just west of the peak of the vertical advection (around 130°W) there is a nodal line of horizontal advection. West of this longitude, contributions of zonal and vertical advection have the same sign. Meridional advection does not have a significant contribution west of 130°W. Thus, in region EQ2 between 130°W and 170°W the SST variations are caused by zonal and vertical advection. West of the dateline, the effects of vertical advection are negligible. In the region EQ3, between 170°W and 150°E, zonal advection seems to be the only dynamical cause of the SST changes. The patterns for zonal and vertical advection in this model compare very closely with the corresponding patterns from the MPIZ model described in M93, but the meridional advection patterns are quite distinct. In the MPIZ model, strong meridional advection in the western and central Pacific seems responsible for the westward shift of the peak in SST anomalies. In the model described in this paper, the westward shift of the SST maximum is not very pronounced.

3.3. A closer look at the individual regions

Figure 10 shows the time series of the model SST anomalies (solid line) and observed SST anomalies (dotted line) in the regions Niño1+2, Niño3 and Niño4 (chosen to allow comparison with the results of M93: see figure 1 therein), while figure 11 shows the model and observed SST anomalies in regions EQ1, EQ2 and EQ3. The model exhibits different dynamical behaviour in these latter regions. A summary of the simulated interannual variability of SST by different ocean models is given in table 3, based on the correlation values between model and observed SST anomalies in the above regions. Model OXA is the present model. It can be seen that ocean models generally have problems in correctly reproducing behaviour near the South American coast (Niño2) and in the west (Niño4). In the central Pacific the values of correlations are generally high. The present model achieves remarkably high values, especially in region EQ2 (0.77). In EQ1 and Niño3 correlations are also good (0.69 and 0.75 respectively). In region Niño2

the correlation is not as good (.44) and the amplitude of anomalies is small compared with observations. In the western Pacific the model performance is poorer, but it is comparable to the results of other ocean models of intermediate complexity (e.g. the Lamont model CZ in table 3).

The model best succeeds in reproducing the interannual variability of SST in the central and eastern Pacific (Niño3, EQ1 and EQ2). However, the model SST anomalies still shows some differences with respect to observations, as can be seen in the time series of figures 10 and 11. In region Niño3 several features can be noted:

(a) the model fails to produce the strong cooling that appears in observations after the 1972/73 event. This is an error shared by other models, as shown in M93.

(b) The model SST anomalies are too low at the begining of the 1982 event, and they are still decreasing at the time the observed SST starts to increase.

(c) As a possible consequence of the former error, the first peak of the 1982 event is very weak (as in other models).

(d) During 1984 different models show similar erroneous behaviour: after the second peak of SST in 1983, most models cool down too much in region Niño3. The error can be located spatially more precisely, if the information in regions EQ1 and EQ2 is taken into account; notice for instance that in our model the 1984 cooling occurs in region EQ2 with extreme intensity, but is absent in region EQ1. After this pronounced cooling, the SST rises again, while the observations are still decreasing. Again, this spurious warming does not happen in the whole region Niño3, but only in the eastern region EQ1.

(e) During 1985 a strong warming tendency is observed in the model, which is weaker in the observations; this difference also seems to appear in other models.

(f) The abrupt cooling that observations show at the end of 1988 in region EQ1 is not well reproduced by the model, in which the cooling occurs almost one year later.

(g) After the cooling of 1988, the observed SST anomalies start increasing in 1989; the model rise of SST occurs later than in observations. This delay in the model warming resembles that in 1982 (cf (c) above). Our model is generally too cool in 1989/90. Busalacchi (private communication) has found a similar error in his model forced by FSU winds, which suggests that there may be errors in the winds.

Among the above discrepancies between model results and observations there are many which are shared with other models. This suggests that the source of the errors may be the common forcing fields, although it is a subject that needs further investigation.

The model fails near the South American coast (Niño1+2), where the anomalies

are very small compared with observations. The low amplitude of the anomalies here may be due to the damping effect that the entrainment parameterization has on Kelvin waves, which in this model do not usually reach the eastern coast. Errors may also be due to the spatial pattern of the upwelling in the model, which is too equatorially confined, with the maximum not close enough to the coast. Thus, even if downwelling Kelvin waves could reach the eastern coast, any warm anomaly in SST produced by the consequent suppression of the climatological upwelling may not be strong.

The response of the model in the western Pacific (Niño4 and EQ3) is not very satisfactory. As discussed in M93, these are regions where processes like vertical mixing of heat and momentum are important. One might expect that GCMs do a better job in these regions than the simple or intermediate models. However, GCMs tend to overstimate the size of the anomalies here, while the present model produces SST of the same magnitude as observations. The timing of the model anomalies is not good though, seemingly delayed with respect to the observations. Particularly noticeable is the delay of the warmings during the '80s and '90s (that is to say, in the events with eastward propagation of SST anomalies). This delay also appears in GCMs.

4. Model results: The heat content

Variations of the model heat content HC are mainly caused by changes in the first layer depth. In general, SST anomalies are only weakly simultaneously correlated with heat content anomalies; only in the eastern equatorial Pacific are HC and SST anomalies highly correlated.

Zebiak (1989) found that heat content anomalies averaged over the equatorial band 5°N to 5°S (all Pacific longitudes) lead the evolution of SST anomalies in region Niño3 by about 3 months. This feature is also found in our results: figure 12a shows that one season before the SST anomalies reach their maximum in region Niño3, heat content anomalies along the equator are unusually high, suddenly decaying by the time that SST anomalies reach their maximum.

Another feature worth noticing is the asymmetry in the heat content between northern and southern hemispheres. The heat content anomalies (averaged along the latitudinal band 5°N to 15°N) are out of phase with those in the band 15°S to 5°S, as can be seen in figure 12b. There seems to be a heat content exchange from the northern hemisphere to the southern hemisphere in the interval between episodes. It is generally a slow process, whose duration and intensity varies from episode to episode. During a warm event the exchange occurs in reverse, with heat transferred back to the northern

hemisphere; only now it is a fast process, and similar in most of the events. Apart from this north/south asymmetry, there is also a strong east-west phase difference. Heat content anomalies in the different regions of the western Pacific (west of 170°W) are positively correlated with each other, but negatively correlated with the regions in the eastern Pacific (east of 170°W). We will return to this point later in this section.

Figure 13 shows the evolution of the equatorial HC anomalies during the 33 years of the integration. It can be seen that the anomalies propagate eastward, although the phase speed is not constant. The evolution of the heat content anomalies at 5°N are shown in figure 14. At this latitude, the heat content anomalies also exhibit clearly propagating features, but this time the propagation is westward. Discontinuities in the propagation of some features are also observed.

The evolution of the equatorial wind anomalies can be seen in figure 15. The zonal stress anomalies propagate eastward during major ENSO events. It seems that waves generated by the central Pacific zonal wind anomalies (as seen in the equatorial HC signal) are generally stronger than the reflected waves. The fact that several Kelvin waves can be excited by winds at different locations in the equatorial Pacific causes irregularities in the free propagation of Kelvin waves from the western boundary, as commented by Chao and Philander (1991).

There are two main possible mechanisms that could account for changes in layer depth: (i) Kelvin / Rossby waves and (ii) local wind forcing. In an attempt to distinguish between these two processes, we focus our attention on autocorrelations of the heat content anomalies (figures 16a and b) and correlations between the heat content anomalies and the zonal wind stress anomalies (figures 16c and d).

The lag correlation r between two variables a_1 and a_2 as a function of time and space is defined as:

$$r(x,\tau) = \frac{\sum_t a_1(x,t+\tau)a_2(t)}{\sqrt{(\sum_t a_1(x,t)^2)(\sum_t a_2(t)^2)}} \qquad ()$$

In each section of figure 16 the variable a_2 is kept fixed in space while a_1 varies in space and time. At negative lags ($\tau < 0$) the variable a_1 leads the evolution of the variable a_2. For the present study, the variable $a_1(x,t)$ represents heat content anomalies (in diagrams 16a and b), or zonal wind stress anomalies (in diagrams 16c and d). Variable a_2 represents the heat content anomalies in region EQ3 in panels a and c, and in region EQ1 in panels b and d. The spatial domain x extends over all

longitudes at the Equator (right half of each panel, west to east) and also all longitudes at 10°N (left half of each panel, east to west). This choice is made because westward off-equatorial Rossby wave signals can connect by reflection with eastward Kelvin wave signals on the equator.

In figure 16a, the heat content anomalies in region EQ3 are positively correlated with the heat content anomalies in the western Pacific at 10°N approximately one to two months earlier. They are also correlated to the equatorial heat content anomalies west of the dateline at lags of -1, 0 and +1 month. This fact could be interpreted as if the state of the ocean in EQ3 were influenced by Rossby waves coming from the central Pacific which reflected off the western boundary as equatorial Kelvin waves. In turn, these Kelvin waves travel eastward and influence the ocean in the equatorial region west of the dateline. The Rossby waves in these western regions can result from anomalies of zonal wind stress in the central Pacific: this is consistent with the correlation between the heat content in region EQ3 and the zonal wind stress at the Equator between 150°E and 140°W (strong and negative) (figure 16c). The winds in the central Pacific also influence the heat content in the eastern Pacific (figure 16d). A striking fact is that the heat content in the eastern regions is not correlated to the heat content in western part of the ocean (figures 16a and b), but is strongly and positively correlated with the wind stress in the central Pacific. From figures 16b and d, it seems clear that the heat content anomalies in the eastern Pacific are mainly due to the wind forcing in EQ3, and not to the Kelvin waves reflected off the western boundary. This fact is illustrated in figure 17a, which shows that the time series of the heat content anomalies in region EQ3 and EQ2 are almost in phase opposition, a fact that contradicts strong direct connection of these regions via Kelvin waves. By contrast, the heat content in region EQ2 exhibits the same evolution as the zonal wind stress in region EQ3, as can be seen in figure 17b. Figure 17c indicates that wave propagation occurs east to the date line between EQ2 and EQ1, and the time series of heat content anomalies in EQ1 approximately lags the time series of heat content in EQ2, with modifications that can be due to local wind forcing.

The former considerations indicate that the western Pacific acts as a reservoir for heat content anomalies, accumulating the contributions of Rossby waves (equatorial and off-equatorial). These Rossby waves are generated by winds in the central Pacific, propagate westward, then reflect off the western boundary as Kelvin waves that rarely can propagate further east than region EQ3. This confinement produces the accumulation of anomalous heat content in the western part of the ocean. At the same time, the regions in the eastern Pacific are influenced by winds in the central and eastern Pacific,

by means of oceanic waves and local forcing respectively. The eastward propagation of HC anomalies during extreme events seems to be related more to the effect of wind anomalies than to the propagation of remotely generated Kelvin waves from the western Pacific.

5. The ENSO cycle from POP analysis

In order to provide a full and concise description of the main features of the simulated ENSO cycle, a POP analysis has been made using the 6 dominant simultaneous EOFs of three fields: model SST anomalies, HC anomalies and observed zonal wind stress anomalies.

The simultaneous POP analysis yields a dominant ENSO-related mode, with a period of about 33 months. This mode explains 38% of the total variance. The POP timeseries are calculated such that the correlation of the imaginary component with the observed SST anomalies in region Niño3 (Niño3 index hereafter) is zero. The real component then corresponds to the *peak* phase of ENSO, while the imaginary part corresponds to the *transition* phase. The correlation of the real time series with the Niño3 index is 0.8, and the real component explains 30% of the total variance, while the imaginary part is weaker, with only 8% of the variance. The lag correlation of the imaginary time series with the Niño3 index has a maximum of 0.6, when the former leads by 3 months, and a minimum of -0.7 at a lag of 9 months, indicating that the ENSO cycle is not symmetric.

The POP time series are shown in figure 18. Positive real values correspond to warm peaks in the free POP cycle, while positive imaginary values correspond to cold-to-warm transitions. The phase progression between real (solid line) and imaginary (dashed line) coefficients looks like a free POP mode during ENSO events, but is incoherent at other times. It can also be seen that the 1982/83 event is not especially dominant, and the amplitude of every El Niño is similar, suggesting that the POP mode represents the common features of the events, and it is not biased by the influence of any specific event. It is notable that during the aborted El Niño of 1975 the time series do not show the characteristic phase of the other warm events.

The spatial patterns of the POP mode are shown in figure 19. The left column shows the real part P (peak phase); the imaginary part Q (transition phase) corresponds to the right column. Panels *a* and *d* show SST anomalies; panels *b* and *e* represent the HC anomalies, and panels *c* and *f* correspond to the zonal stress anomalies. The POP technique allows a simple interpretation of these patterns and their time evolution,

which is represented by the cycle $Q \rightarrow P \rightarrow -Q \rightarrow -P \rightarrow Q \ldots$

For SST, the variance of the peak phase is clearly larger than the transition phase. The spatial configuration of SST anomalies during the peak phase shows a maximum in the equatorial region EQ1 and EQ2, smoothly decaying toward the east and the west. This pattern has the same sign over most of the domain, except in the west Pacific area. This mode has a wider latitudinal extension in the region EQ1. Notice that this configuration is similar to the observed pattern of the observed SST anomalies (Latif et al. 1993), except that the latter has its widest latitudinal extent along the South American coast, and everywhere is broader than the model results.

For heat content anomalies, both transition and peak phase anomalies have similar size. The peak phase pattern illustrates a west-east split, and has the appearance of a dipole, with anomalies in the eastern Pacific of different sign to those in the western Pacific. The transition phase pattern is characterized by a north/south asymmetry: heat content anomalies along the equator and southern hemisphere appear to be in phase opposition with the anomalies in the northern hemisphere.

In the zonal wind field, the peak phase of ENSO is characterized by a maximum centered on the equator, to the west of the SST maximum. On the other hand, during the transition phase, the largest wind anomalies are off equatorial, and are located in the western Pacific north of the Equator.

The POP mode found for the present model is very similar to the low frequency mode found by Latif et al. (1993) in the POP analysis of the observed fields, regarding both spatial patterns and time scale.

The POP interpretation for the pattern evolution, together with the information discussed in previous sections, leads to the following description of the evolution of an ENSO event in our model.

Cold Phase (patterns -P):

Easterly wind anomalies are present in regions EQ2 and EQ3. According to linear therory, they induce downwelling Rossby waves in the regions to the west, and upwelling Kelvin waves in the regions to the east. The Rossby waves propagate westward, and reflect off the boundary as Kelvin waves. These new downwelling Kelvin waves propagate eastward into the region EQ3, where they are opposed by the easterly wind anomalies. In this way, positive anomalies of heat content are accumulated in the western Pacific. The eastern Pacific is dominated by the upwelling Kelvin waves excited by the winds in the central

Pacific. These waves are associated with negative anomalies of heat content. Consequently, in this phase, there is a strong zonal gradient in the heat content anomaly.

The winds in the central Pacific also induce stronger westward oceanic currents, which will decrease the SST in the central ocean by transporting cold water from the east. In the eastern Pacific there is increased upwelling, caused by horizontal divergence and by the upwelling Kelvin waves influence. This upwelling will contribute to the cooling of the surface water in the east.

Cold-to-warm onset phase (patterns Q):

About 8 months later, the equatorial anomalies of zonal wind weaken; the wind anomalies become positive over the western Pacific, especially north of the Equator (5°N) where anomalies are larger than the equatorial ones.

The main effect of the weakening of the easterlies is to allow eastward propagation of the positive heat content anomalies accumulated in the western Pacific, so that the equatorial ocean becomes homogeneous and positive with respect to HC. The positive anomalies of HC in the eastern Pacific are favoured by the Kelvin waves generated in region EQ2 by slackening of the easterly winds there.

The heat content in the north western Pacific decreases and become negative with the arrival of Rossby waves (created by the westerly wind in EQ3) together with the equatorward mass transport as an Ekman response to the positive wind anomalies. so producing the meridional gradient characteristic of this transition phase. The Ekman contribution is caused by the positive stress anomalies in 5°N, which produce negative anomalies of HC at $10° - 15°$N. This scenario is consistent with Wakata and Sarachik (1991). It seems that all these features are produced not only by waves, but also by direct wind-driven oceanic transport.

The eastern Pacific is still dominated by negative SST anomalies, although weak positive anomalies appear in EQ1 and EQ2. In EQ1 the warming is produced by suppression of upwelling, while in EQ2 the warming is due to changes in zonal advection (weaker currents and weaker temperature gradients).

Mature warm phase of the event (patterns P):

The positive anomalies of the wind has its maximum over the equatorial central Pacific. These westerlies enhance the depression of the thermocline in the east, contributing to the positive heat content anomalies there. At the same time, more Rossby waves are created, which propagate to the western boundary and reflect as negative Kelvin waves which will be stopped by the winds in EQ3 and EQ2 as before. The negative anomalies of heat content are thus confined

to the western Pacific. The meridional gradient in HC has been replaced by a zonal one.

The SST anomalies in EQ1 and EQ2 have increased, and are now anomalously high, and dominate the central and eastern Pacific. It seems that these anomalies have expanded both eastward and westward. The maximum SST anomalies are located in EQ2 and EQ1.

Decay of the warm event, cold onset (patterns -Q):

The positive equatorial anomalies of the zonal wind stress weaken, and so does the zonal gradient of heat content anomalies in the equator. As a result, there is propagation of negative HC anomalies along the equator.

The positive SST anomalies still propagate to the date line. In the eastern Pacific, the first negative anomalies appear. The warm event has finished and a cold event has started to develop.

In the western Pacific north of the equator, intense negative wind anomalies produce the accumulation of off-equatorial positive HC anomalies. These constitute an incipient reservoir of energy for the next warm event.

In this description the evolution is assumed to follow a POP cycle, with no decay and no asymmetry between warm and cold events. Note that although by construction a POP mode need not be consistent with ocean dynamics, many features of the ENSO POP discussed here are dynamically consistent, and help explain the response of the ocean to the wind forcing. Further, the wind anomalies of the POP mode are consistent with the SST anomalies, so that the POP mode could be used to train a statistical atmosphere (cf Balmaseda 1993, Balmaseda et al. 1994).

6. Conclusions

An ocean model of intermediate complexity has been used to simulate interannual variability in the Pacific, using observed winds during the period 1961-1993. The model reproduces the interannual evolution of SST over the central Pacific well.

The thermodynamic processes involved in the development of the SST anomalies are investigated. In the central region EQ2 the main mechanism is zonal advection: during warm ENSO events, warming in EQ2 is caused by the weakening of the zonal currents and the weakening of the zonal SST gradients. In the eastern region EQ1, the main cause of warming is the reduction in the upwelling, caused both by Kelvin waves and by local forcing. Near the South American coast the model response is poorer, probably due to the parameterization of the upwelling, which damps Kelvin waves too strongly and prevents them from reaching the coast. The model SST anomalies do

not match observations in the western Pacific well: although the causes of such failure are difficult to identify, probably the surface heat flux (here simply parameterised as a negative feedback) is important. The anomalies of SST in the model during El Niño years first appear in the regions EQ1 and EQ2, and then expand to the east and west. The eastward propagation is partially inhibited, as noted above. In the strong 1982/83 event, the warm anomalies first appear in the region EQ2, and then propagate eastward. In observations, the warming in some events first happens very near the coast, and then expands into the central Pacific. Warming over the western Pacific is very weak, and usually happens six or more months before the main warming in the east.

The ENSO phenomenon can be described as a cycle in the context of SST, HC and wind stress anomalies. During the peak phase of ENSO (warm or cold events), there is a strong zonal gradient of HC anomalies, in such a way that the spatial distribution of HC anomalies appears as a dipole, with anomalies of different sign in the eastern and western Pacific: during warm events, the anomalies are positive in the east and negative in the west; vice versa for cold events. The winds over the central Pacific contribute to the formation of these gradients in different ways: (a) by the generation of Rossby and Kelvin waves of different signs which propagate westward and eastward respectively; (b) by inhibiting the propagation of Kelvin waves from the western boundary as a result of the reflection of the Rossby waves there; (c) the winds inhibit the propagation of Rossby waves coming from the eastern boundary. In this way, anomalies of different sign are separated and confined at both sides of the basin.

During the transition phase of ENSO, the equatorial wind anomalies weaken, so that the anomalies of HC confined in the western Pacific are released and spread eastward along the equator. The largest wind anomalies have moved to the north in the western Pacific and contribute to the accumulation of HC anomalies in the northern Pacific, which have opposite sign to those along the Equator. In this way, the strong zonal gradient in HC anomalies characteristic of the peak phase is replaced by a meridional gradient during the transition phase.

In agreement with the scenario proposed by Wakata and Sarachik (1991), the propagation of the model HC anomalies along the equator occur when the zonal wind anomalies weaken. The appearance of anomalies in the northern ocean in the transition phase is related to the propagation of Rossby waves coming from the eastern and central Pacific as well as to local Ekman dynamics associated with strong wind anomalies.

The above description accounts for several observed features of ENSO: the exchange of heat between hemispheres during the ENSO cycle, the eastward propagation

of sea level anomalies along the equator, and the westward propagation of sea level anomalies along the northern Pacific. It seems that all these features are produced by a combination of waves and direct oceanic transport.

Allen, M.R., 1992: Interactions between the atmosphere and oceans on time-scales of weeks to years. PhD thesis, University of Oxford, 202 pages

Anderson, D.L.T. and McCreary, J.P., 1985: Slowly propagating disturbances in a coupled ocean-atmosphere model. *J. Atmos. Sci.* **42** 615-629.

Balmaseda, M.A., 1993: Simulación y predicción del fenómeno *ENSO* con un modelo acoplado océano-atmósfera. PhD thesis, University of Alcalá de Henares, Spain

Balmaseda, M.A., Anderson, D.L.T., and Davey M.K., 1994: ENSO prediction using a dynamical ocean model coupled to statistical atmospheres. *Tellus* in press.

Battisti, D.S. and Hirst, A.C., 1989: Interannual variability in a tropical atmosphere-ocean model: influence of the basic state, ocean geometry and non-linearity. *J. Atmos. Sci.* **46** 1687-1712.

Bjerknes, J., 1966: A possible response of the atmospheric Hadley circulation to equatorial anomalies of temperature. *Tellus* **18** 820-828.

Bjerknes, J., 1969: Atmospheric teleconnections from the equatorial Pacific. *Mon. Wea. Rev.* **97** 163-172.

Blumenthal, M.B., 1991: Predictability of a coupled ocean-atmosphere model. *J. Climate* **4** 766-784.

Busalacchi, A.J. and O'Brien, J.J., 1980: The seasonal variability in a model of the tropical Pacific. *J. Phys. Oceanogr.* **10** 1929-1951.

Busalacchi, A.J., Takeuchi, K., and O'Brien, J.J., 1983: Interannual variability of the equatorial Pacific. Hydrodynamics of the Equatorial Ocean. J.C.JNihoul, Ed., Elsevier Oceanogr. Ser., Vol. 36.

Cane, M.A., 1984: Modeling sea level during El Niño. *J. Phys. Oceanogr.* **14** 1864-1874.

Chao Y., and Philander S.G.H., 1991: On the structure of the Southern Oscillation and evaluation of coupled ocean-atmosphere models. *TOGA notes* **3** 1-8.

Giese, B.S. and Harrison, D.E., 1990: Aspects of the Kelvin wave response to episodic wind forcing. *J. Geophys. Res.* **95** 7289-7312.

Gill, A.E., 1983: An estimation of sea-level and sea-current anomalies during the 1972 El Niño and consequent thermal effects. *J. Phys. Oceanogr.* **13** 586-605.

Goldenberg B., and O'Brien J., 1981: Time and space variability of Tropical Pacific wind stress. *Mon. Wea. Rev.* **109** 1190-1207.

Hasselmann, K., 1988: PIPS and POPs: The reduction of complex dynamical systems using Principal Interaction and Oscillation Patterns. *J. Geophys. Res.* **93(D9)** 11015-11021.

Hirst, A.C., 1986: Unstable and damped equatorial modes in simple coupled ocean-atmosphere models. *J. Atmos. Sci.* **43** 606-630.

Latif, M., Sterl, A., Maier-Reimer E., and Junge, M.M., 1993: Climate variability in a coupled GCM. Part 1: the tropical Pacific. *J. Climate* **6** 5-21.

McCreary, J.P., 1983: A model of tropical ocean-atmosphere interaction. *Mon. Wea. Rev.* **111** 370-387.

McCreary, J.P. and Anderson, D.L.T., 1984: A simple model of El Niño and the Southern Oscillation. *Mon. Wea. Rev.* **112** 934-946.

McCreary, J.P. and Anderson, D.L.T., 1991: An overview of coupled ocean-atmosphere models of El Niño and the Southern Oscillation. *J. Geophys. Res.* **96** 3125-3150.

McCreary, J.P. and Kundu, P.K., 1988: A numerical investigation of the Somali current during the southwest monsoon. *J. Mar. Res.* **46** 25-58.

Miller, A.J., Barnett, T.P., Graham, N.E., 1993: A comparison of some ocean models: hindcast skill and El Niño evolution. *J. Phys. Oceanogr.* **23** 1567-1591.

Neelin, J.D., 1989: Interannual oscillations in an ocean general circulation model coupled to a simple atmosphere model. *Phil. Trans. R. Soc. Lond.* **329** 189-205.

Neelin, J.D., Latif, M., and Jin F.-F., 1994: Dynamics of coupled ocean-atmosphere models: the tropical problem. *Ann. Rev. Fluid Mech.* to appear.

Philander, S.G.H. and Seigel, A.D., 1985: Simulation of El Niño of 1982-83. In: Coupled ocean-atmosphere models(J. Nihoul ed.), pp 517-541, Elsevier, Amsterdam.

Rennick, M.A. and Haney, R.L., 1986: Stable and unstable air-sea interactions in the equatorial region. *J. Atmos. Sci.* **43** 2937-2943.

Reynolds, R.W., 1988: A real-time global sea surface temperature analysis. *J. Climate* **1** 75-86.

Reynolds, R.W., and Marsico, D.C., 1993: An improved real-time global sea surface temperature analysis. *J. Climate* **6** 114-119.

Schopf, P.S. and Harrison, D.E., 1983: On equatorial waves and El Niño. I: Influences of initial states on wave-induced currents and warming. *J. Phys. Oceanogr.* **13** 936-948.

Schopf, P.S. and Suarez, M.J., 1988: Vacillations in a coupled ocean-atmosphere model. *J. Atmos. Sci.* **45** 549-566.

Seager, R., 1989: Modeling tropical Pacific sea surface temperature: 1970-87. *J. Phys. Oceanogr.* **19** 419-434.

Stockdale, T.N., 1992: Simulation and prediction of tropical SST with a coupled ocean-atmosphere model. PhD thesis, Oxford University, UK

Stockdale, T.N. et al, 1993: Intercomparison of tropical ocean GCMs. WCRP-79, WMO/TD-No545, 90pp.

Wakata, Y. and Sarachik, E.S., 1991: On the role of equatorial ocean modes in the ENSO cycle. *J. Phys. Oceanogr.* **21** 434-443.

Wu, D.H., Anderson D.L.T., and Davey M.K., 1994: ENSO prediction experiments using a simple ocean-atmosphere model. *Tellus.* In press.

Xie, S., Kubokawa, A. and Hanawa, K., 1989: Oscillations with two feedback processes in a coupled ocean-atmosphere model. *J. Climate* **2** 946-964.

Xu, J-S. and von Storch, H., 1990: Predicting the state of the Southern Oscillation using Principal Oscillation Pattern analysis. *J. Climate* **3** 1316-1329.

Yamagata, T. and Masumoto, Y., 1989: A simple ocean-atmosphere coupled model for the origin of a warm ENSO event. *Phil. Trans. Roy. Soc. London* **A329** 225-236.

Zebiak, S.E., 1989: Oceanic heat content variability and El Niño cycles. *J. Phys. Oceanogr.* **19** 475-486.

Zebiak, S.E. and Cane, M., 1987: A model El Niño Southern Oscillation. *Mon. Wea. Rev.* **115** 2262-2278.

Tables

Table 1: Values of parameters used in the ocean model.

Variable	Value	Description
H_e	100 m	entrainment depth
H_d	100 m	detrainment depth
t_e	1 day	time scale for entrainment
t_d	500 days	time scale for detrainment
ν	$500 m^2/s$	horizontal viscosity
κ	$500 m^2/s$	thermal diffusivity
ζ	$500 m^2/s$	horizontal mixing
C_D	0.0015	drag coefficient
μ	.5	wind reduction factor
γ	0.75	upwelling coefficient
β	$2.28 \times 10^{-11} m^{-1} s^{-1}$	Coriolis gradient

Table 2: Ocean regions.

Region	Longitude	Latitude
Niño1	90 W - 80 W	5 S - 10 S
Niño2	90 W - 80 W	0 - 5 S
Niño3	150 W - 90 W	5 N - 5 S
Niño4	160 E - 150 W	5 N - 5 S
EQ3	150 E - 170 W	5 N - 5 S
EQ2	170 W - 130 W	5 N - 5 S
EQ1	130 W - 90 W	5 N - 5 S

Table 3: Summary of correlations between observed and model SST anomalies for 1970 to 1985, simulated by 5 different models, for different regions of the Equatorial Pacific. The present model is OXA. Values for the first 4 models are taken from Table 1 in Miller et al (1993). For OXA* values are for 1965-1993.

	EQ3	Niño 4	EQ2	Niño 3	EQ1	Niño 2
CZ	—	.46	—	.60	—	.68
MPIZ	—	.76	—	.74	—	.59
OPYC	—	.72	—	.63	—	.46
GFDL	—	.81	—	.69	—	.57
OXA	.31	.56	.74	.72	.70	.50
OXA*	.28	.59	.77	.75	.69	.44

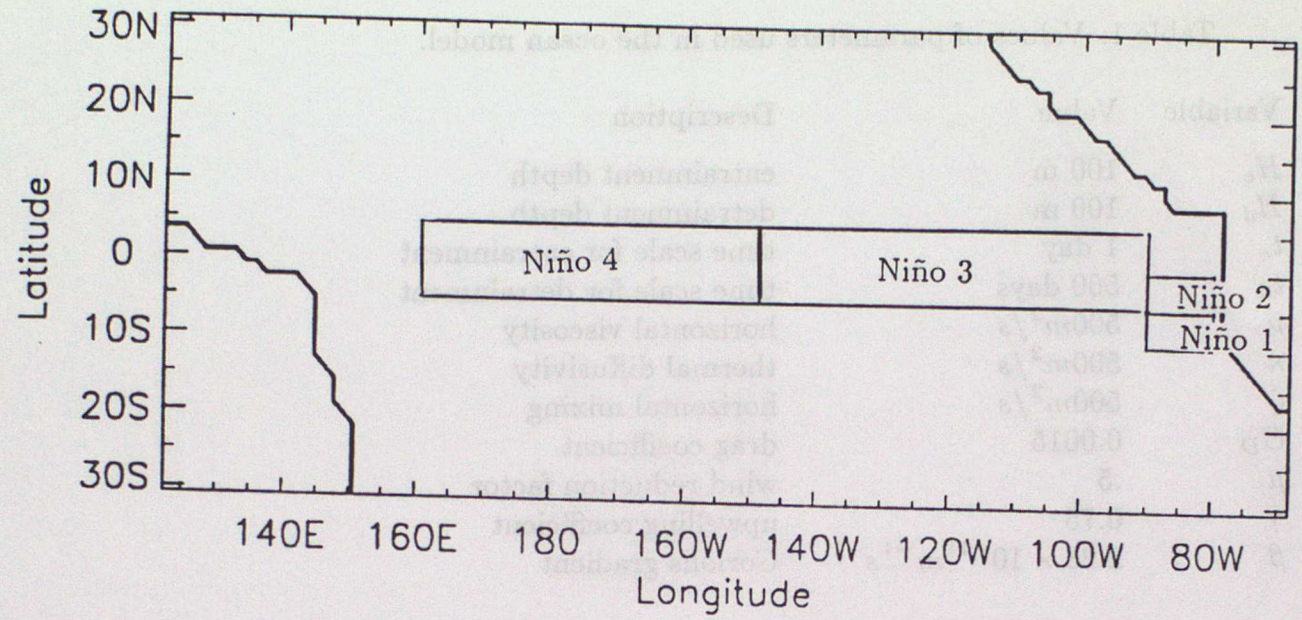

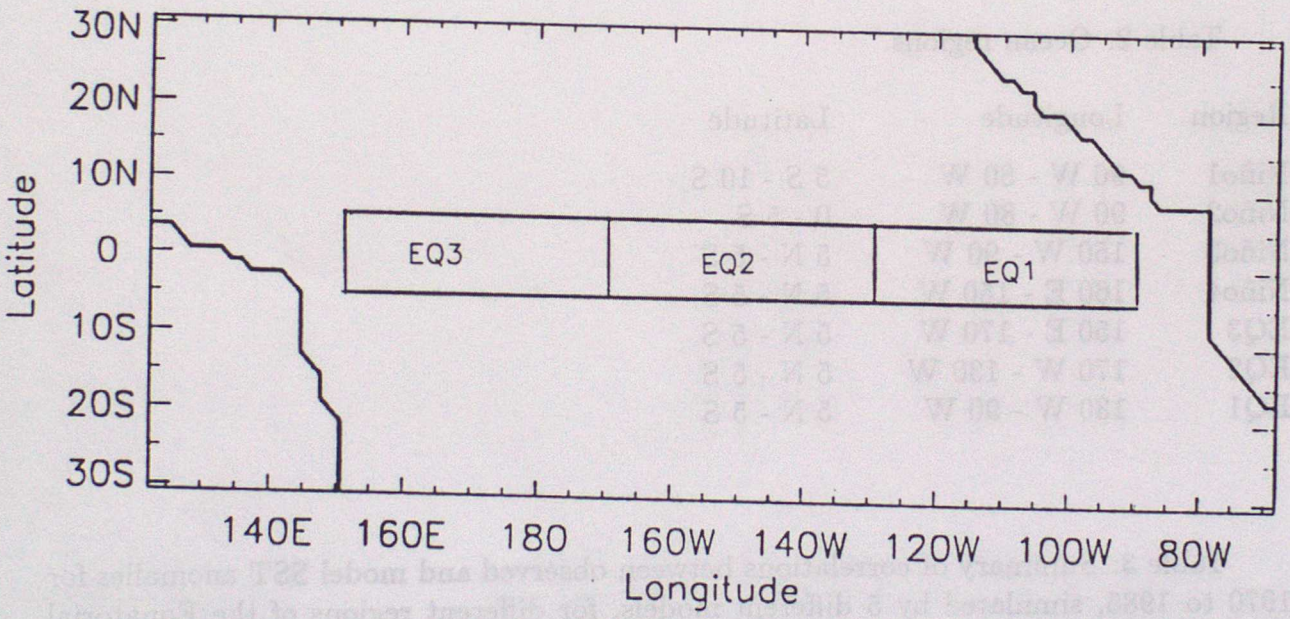

Fig. 1: Location of the different oceanic regions used in the analysis.

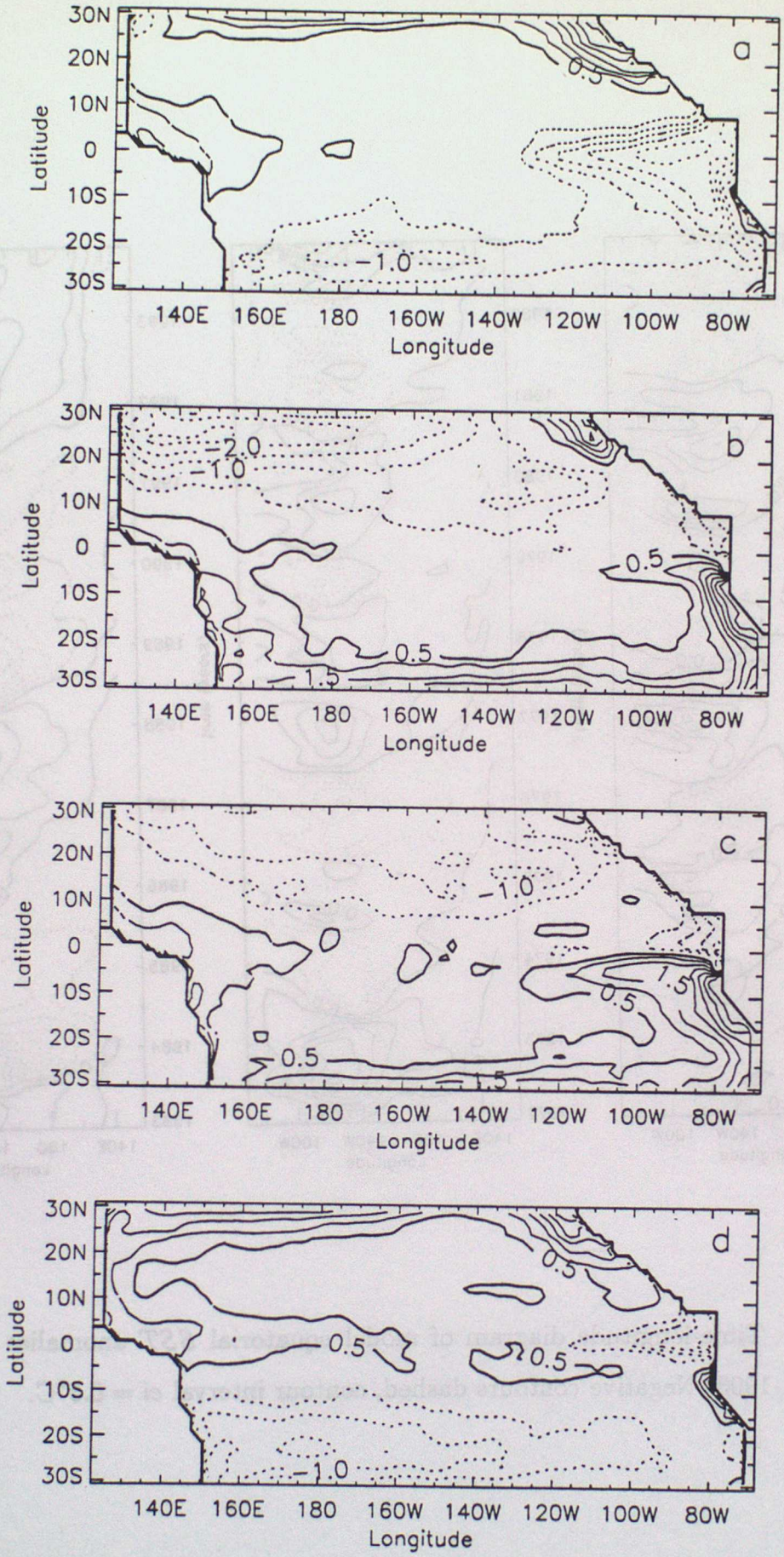

Fig. 2: Difference (model minus observed) between SST model climatology and observed COADS climatology; (a) March, (b) June, (c) September and (d) December. (Negative contours dashed, no zero contour: contour interval $ci = 0.5°C$).

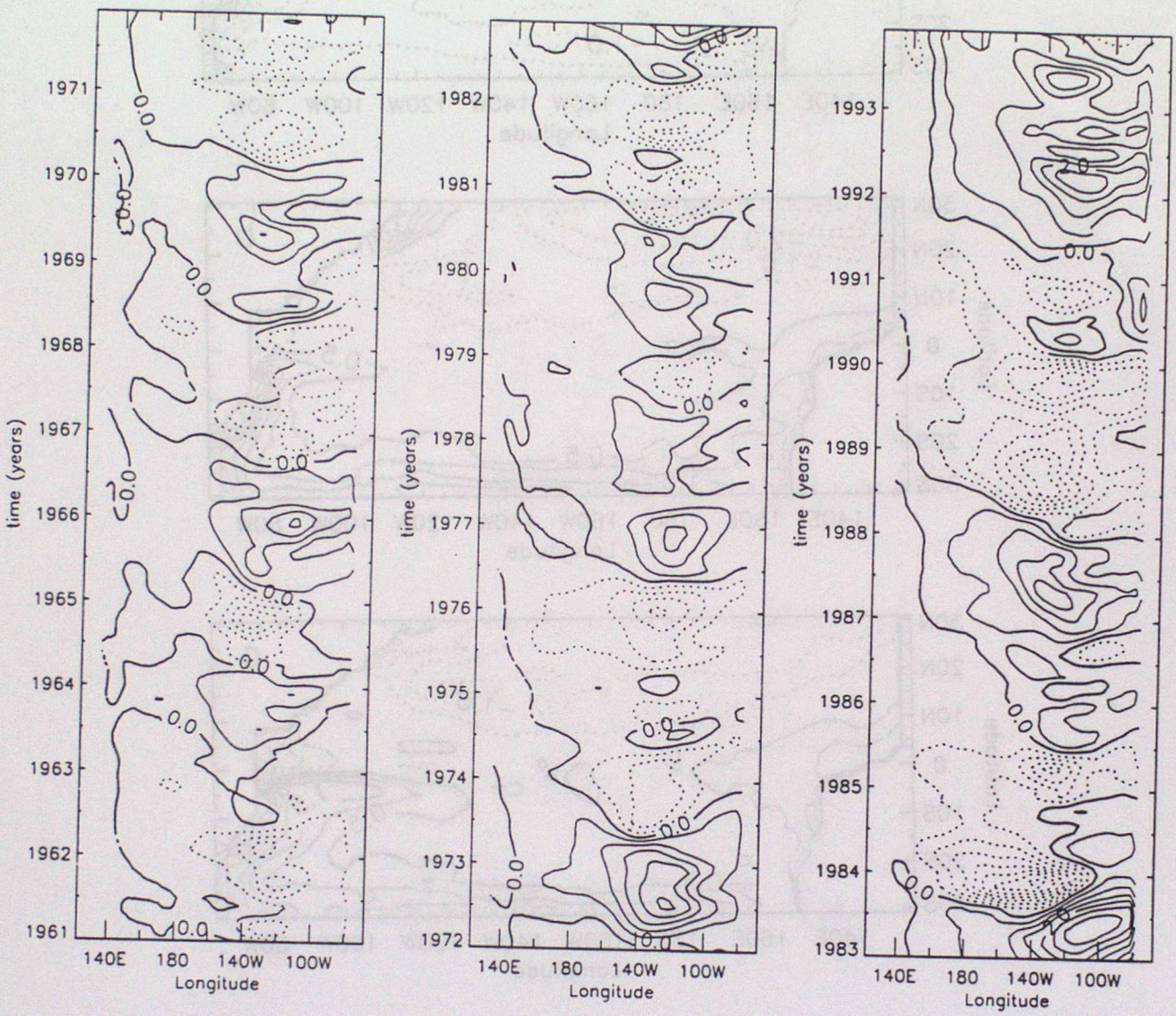

Fig. 3a: Time-longitude diagram of model equatorial SST anomalies during the period 1961-1993. Negative contours dashed, contour interval $ci = 0.5°C$.

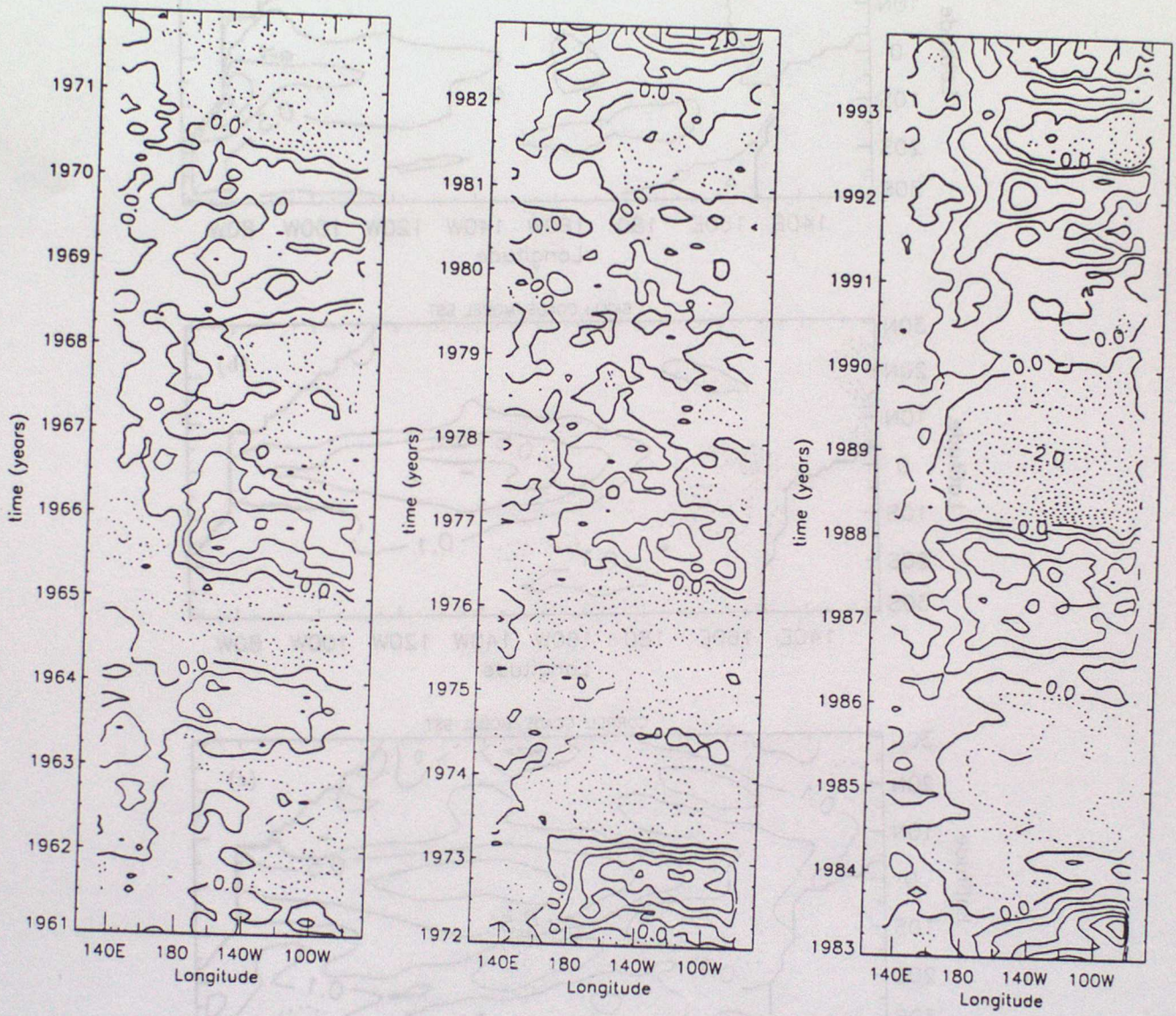

Fig. 3b: Time-longitude diagram of observed equatorial SST anomalies during the period 1961-1993. Negative contours dashed, contour interval $ci = 0.5°C$.

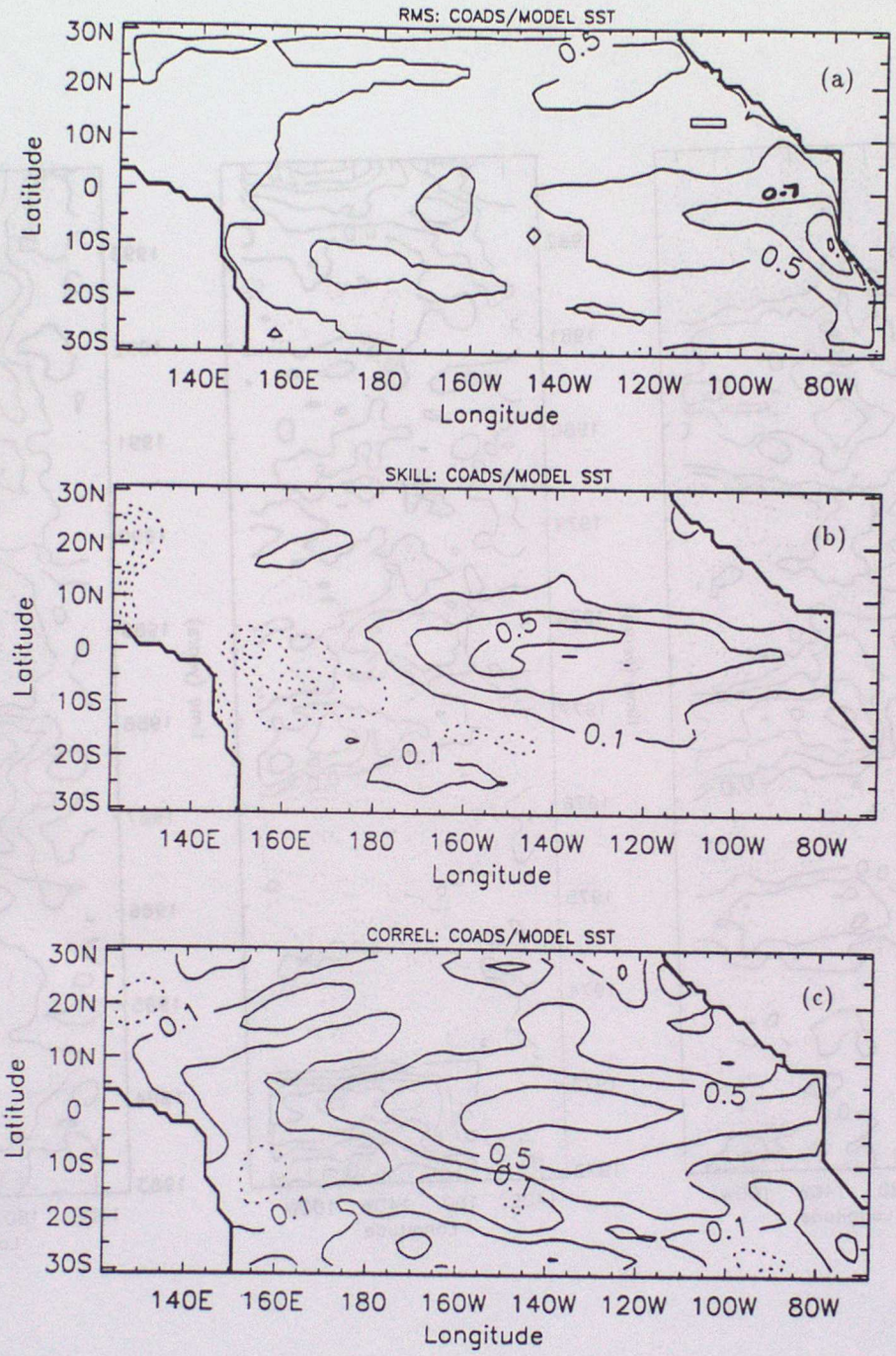

Fig. 4: Statistics for the model SST anomalies relative to COADS observations; (a) RMS error ($ci = 0.2°C$), (b) hindcast skill S ($ci = 0.2$), (c) correlation ($ci = 0.2$). Negative contours dashed, no zero contour.

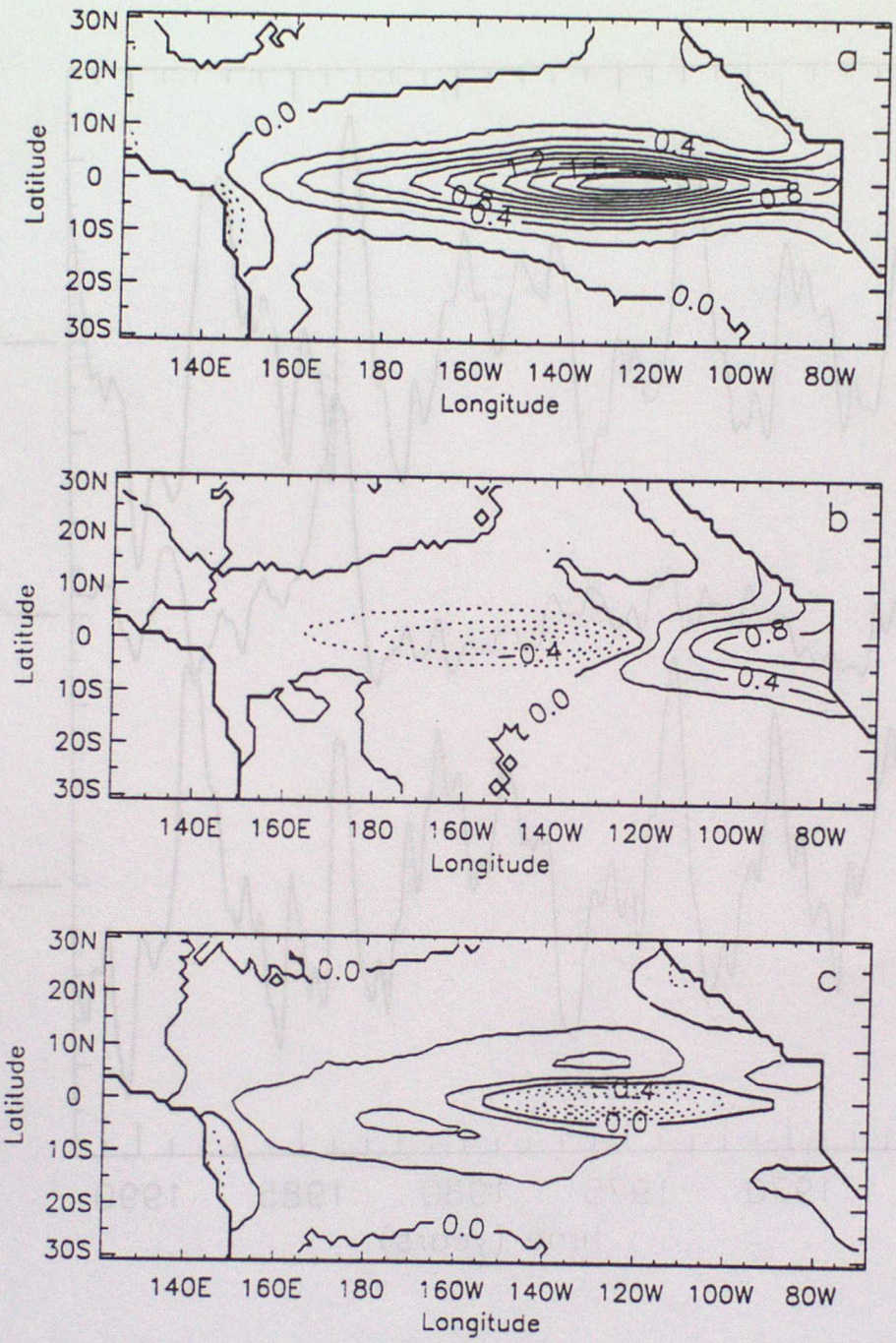

Fig. 5: Empirical orthogonal functions for the model *SST* anomalies: (a) EOF1, 59% of total variance, (b) EOF2 13%, (c) EOF3 10%. ($ci = 0.2$ arbitrary units. The EOFs are scaled by the variance explained by each mode).

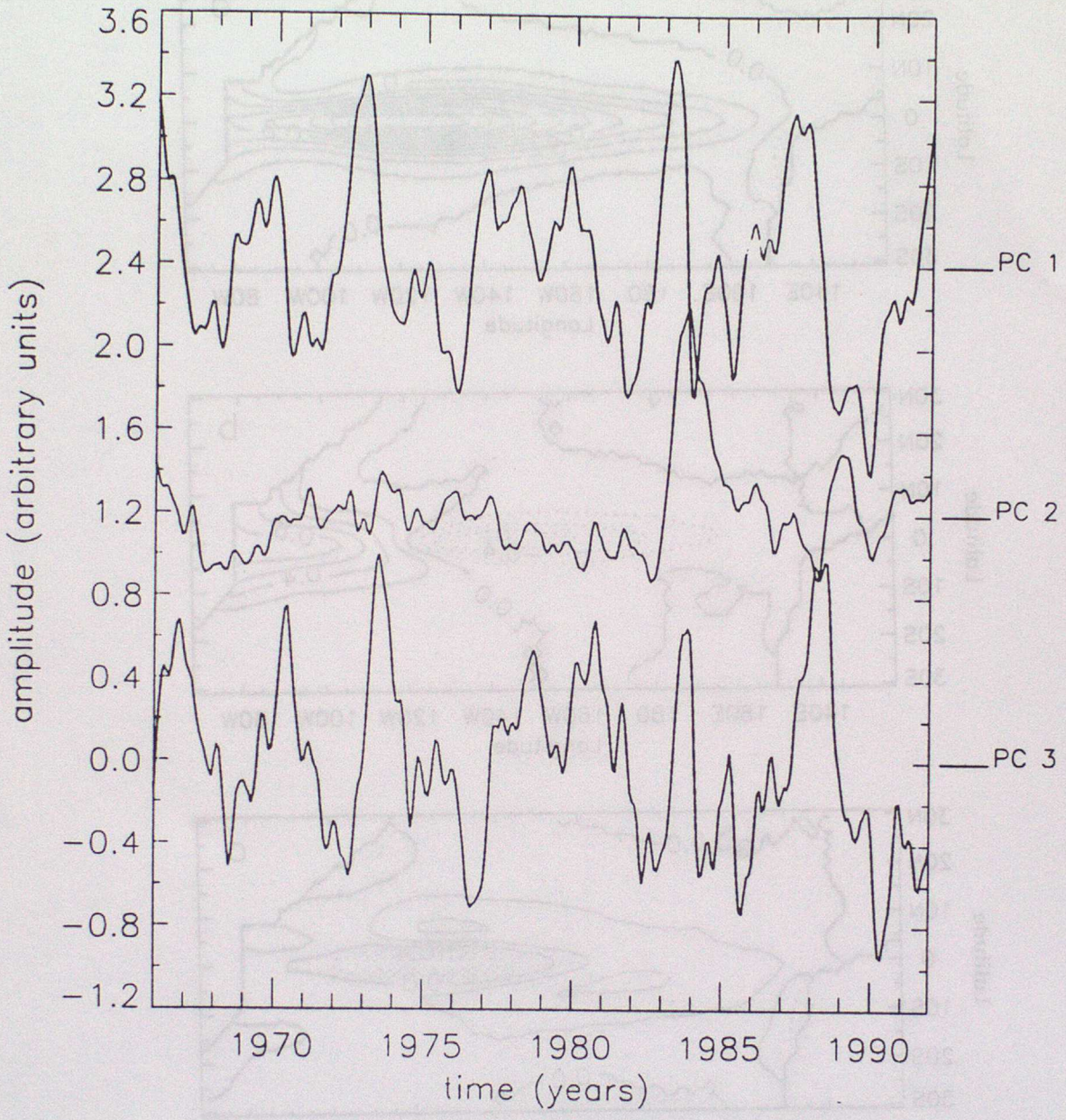

Fig. 6: Time series (Principal Components PC) for the model *SST* EOF patterns: PC1 (top), PC2 (middle), PC3 (bottom). Note the consistent phase difference between PC1 and PC3.

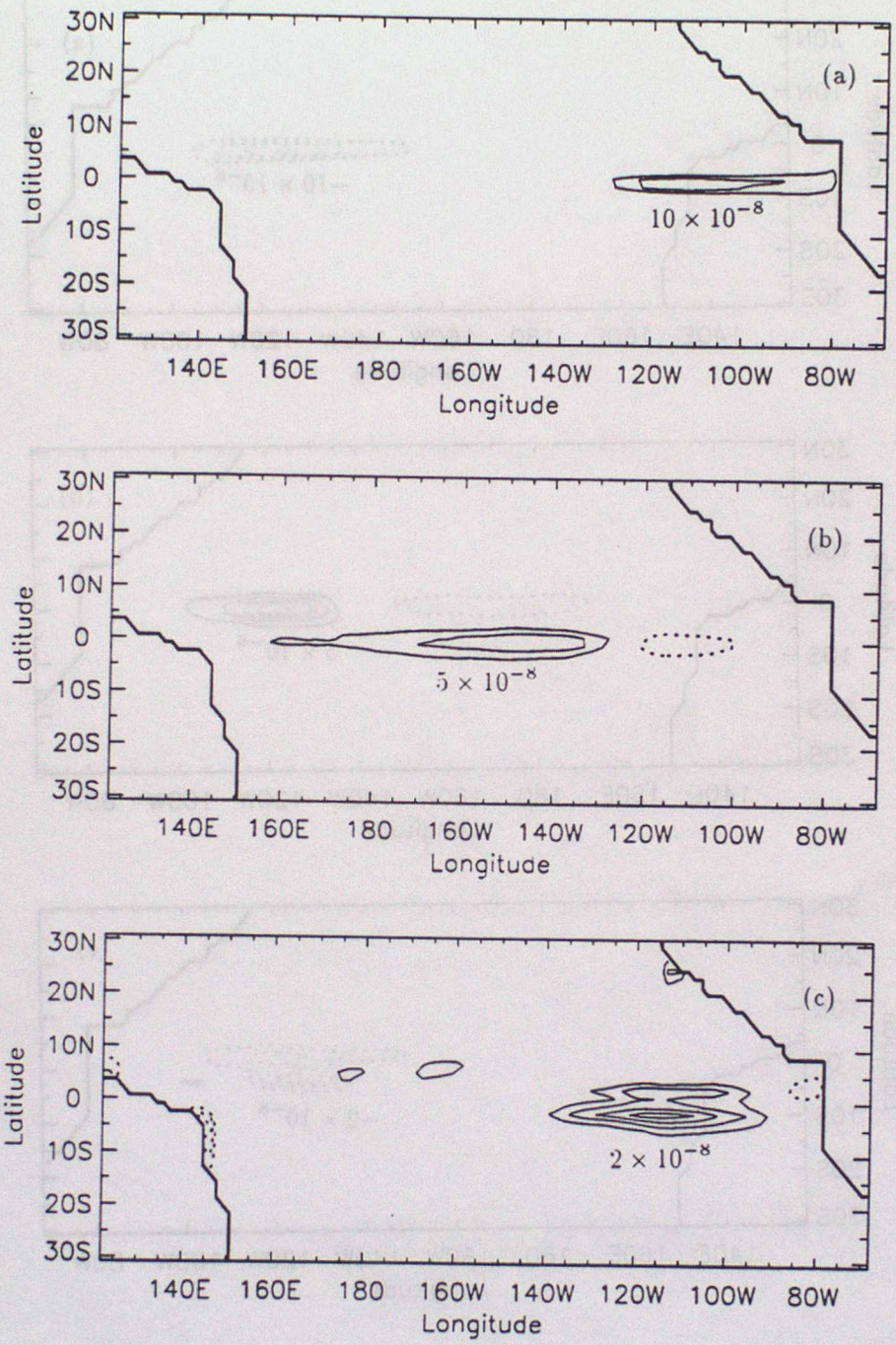

Fig. 7: Advection patterns associated with EOF1 of model SST: (a) APW_1 (vertical), $ci = 10 \times 10^{-8} K/s$; (b) APU_1 (zonal), $ci = 5 \times 10^{-8} K/s$; (c) APV_1 (meridional), $ci = 2 \times 10^{-8} K/s$. Negative contours dashed, zero contour omitted.

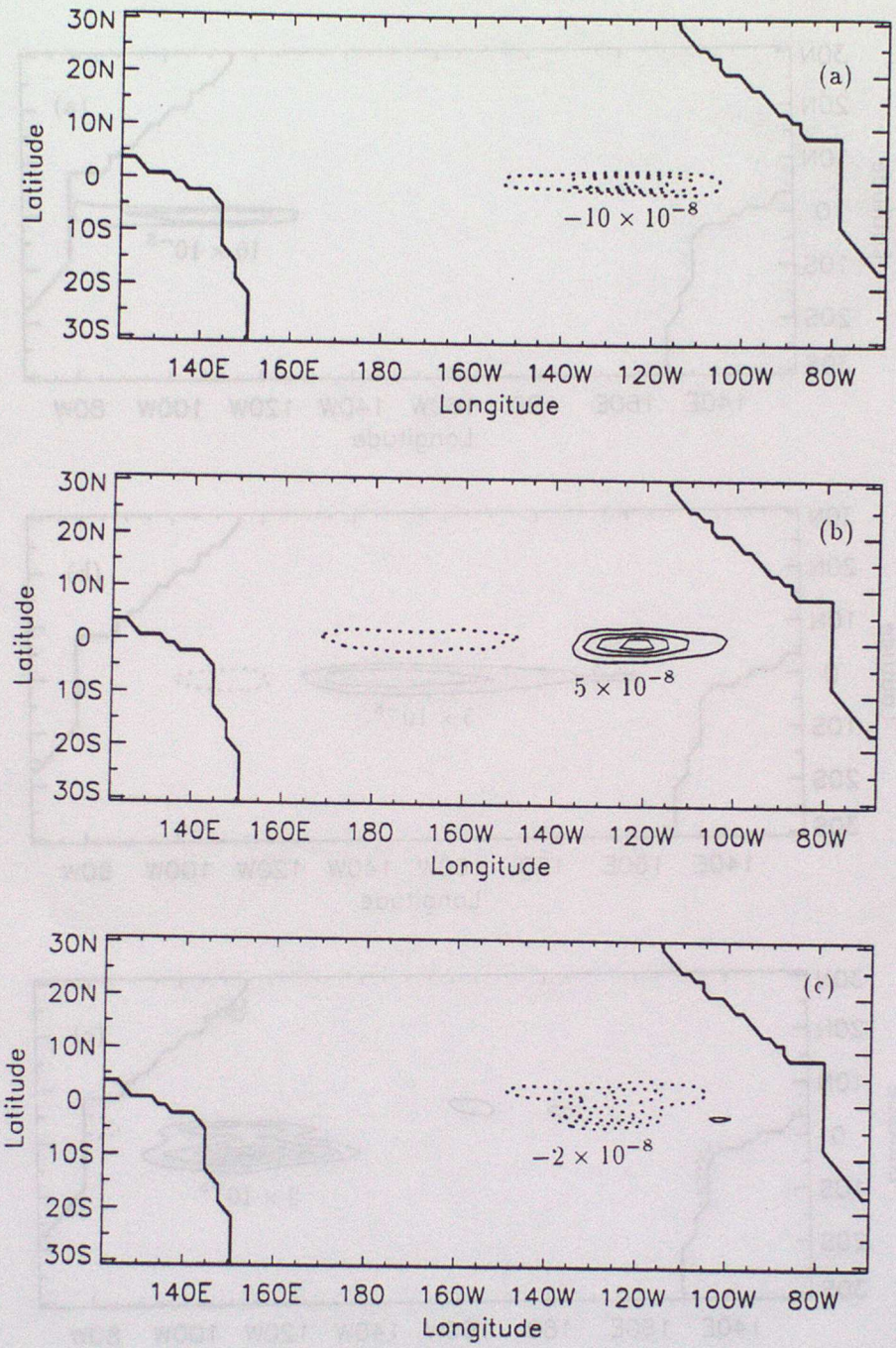

Fig. 8: Advection patterns associated with EOF2 of model SST: (a) APW_2 (vertical), $ci = 10 \times 10^{-8} K/s$; (b) APU_2 (zonal), $ci = 5 \times 10^{-8} K/s$; (c) APV_2 (meridional), $ci = 2 \times 10^{-8} K/s$. Negative contours dashed, zero contour omitted.

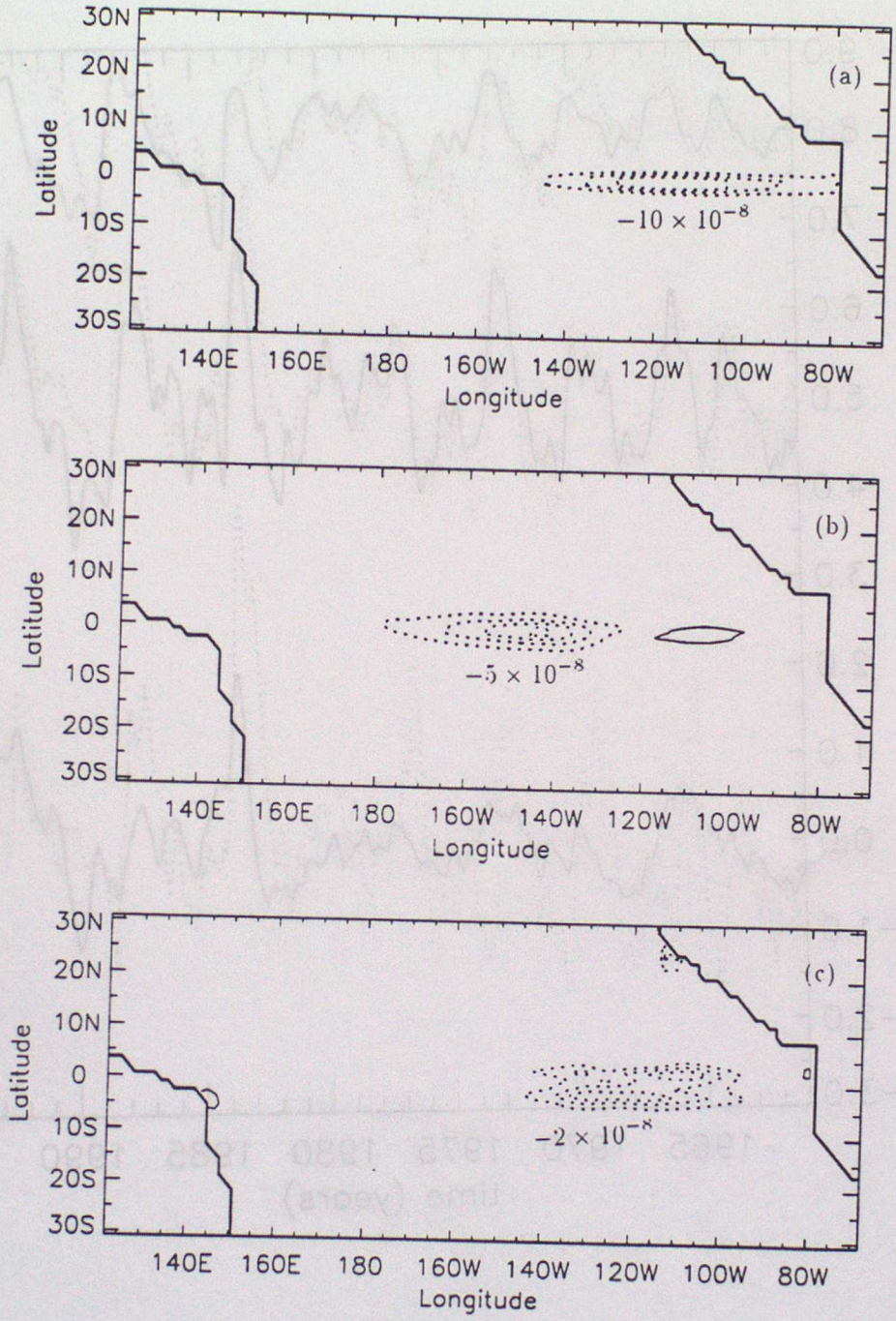

Fig. 9: Advection patterns associated with EOF3 of model SST: (a) APW_3 (vertical), $ci = 10 \times 10^{-8} K/s$; (b) APU_3 (zonal), $ci = 5 \times 10^{-8} K/s$; (c) APV_3 (meridional), $ci = 2 \times 10^{-8} K/s$. Negative contours dashed, zero contour omitted.

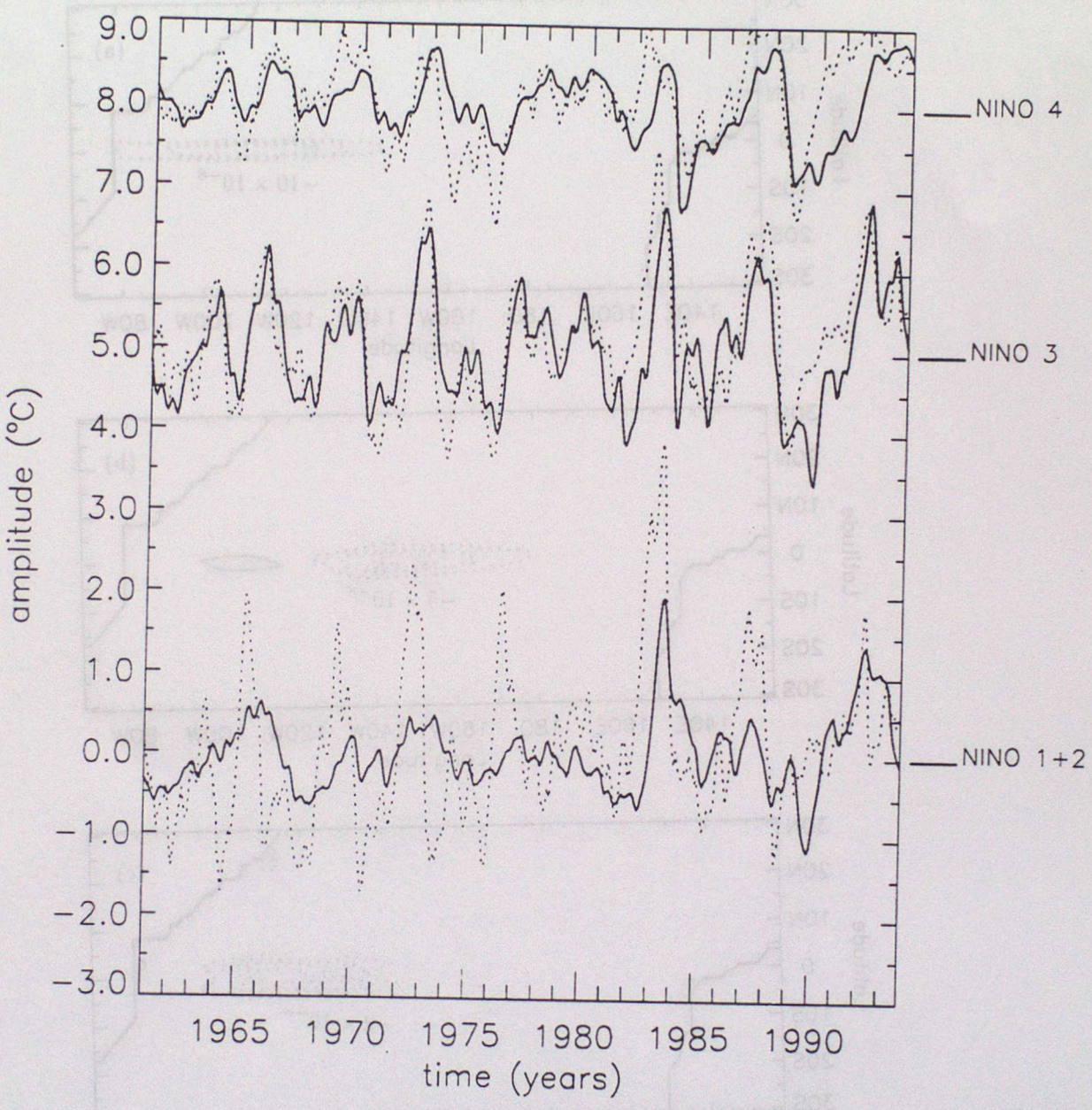

Fig. 10: Time evolution of SST anomalies in regions Niño1+2, Niño3 and Niño4, from the ocean model (solid line) and from observations (dotted line). The zero line for regions Niño3 and Niño4 has been displaced to 5°C and 8°C respectively.

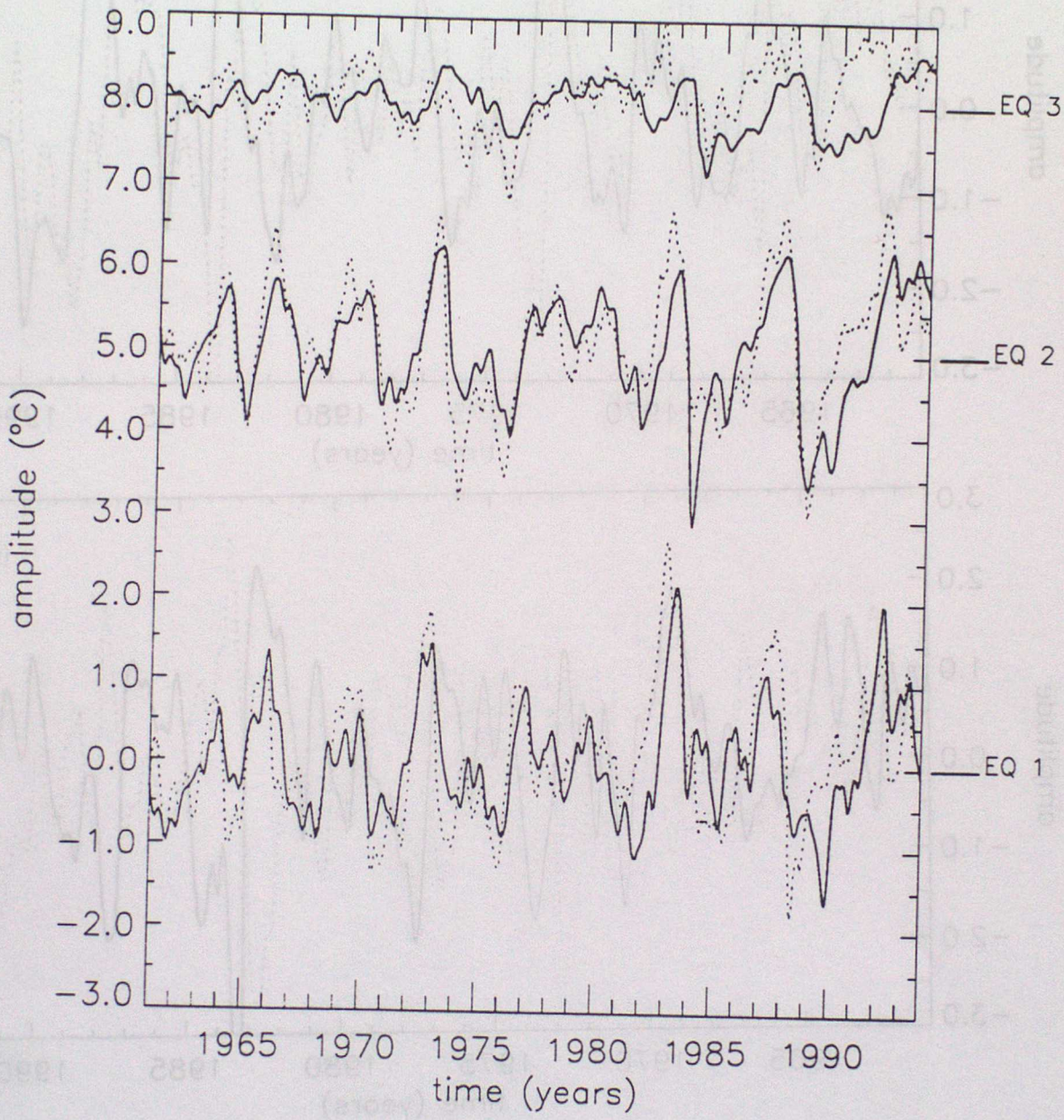

Fig. 11: Time evolution of *SST* anomalies in regions EQ1, EQ2 and EQ3, from the ocean model (solid line) and from observations (dotted line). The zero line for regions EQ2 and EQ3 has been displaced to 5°C and 8°C respectively.

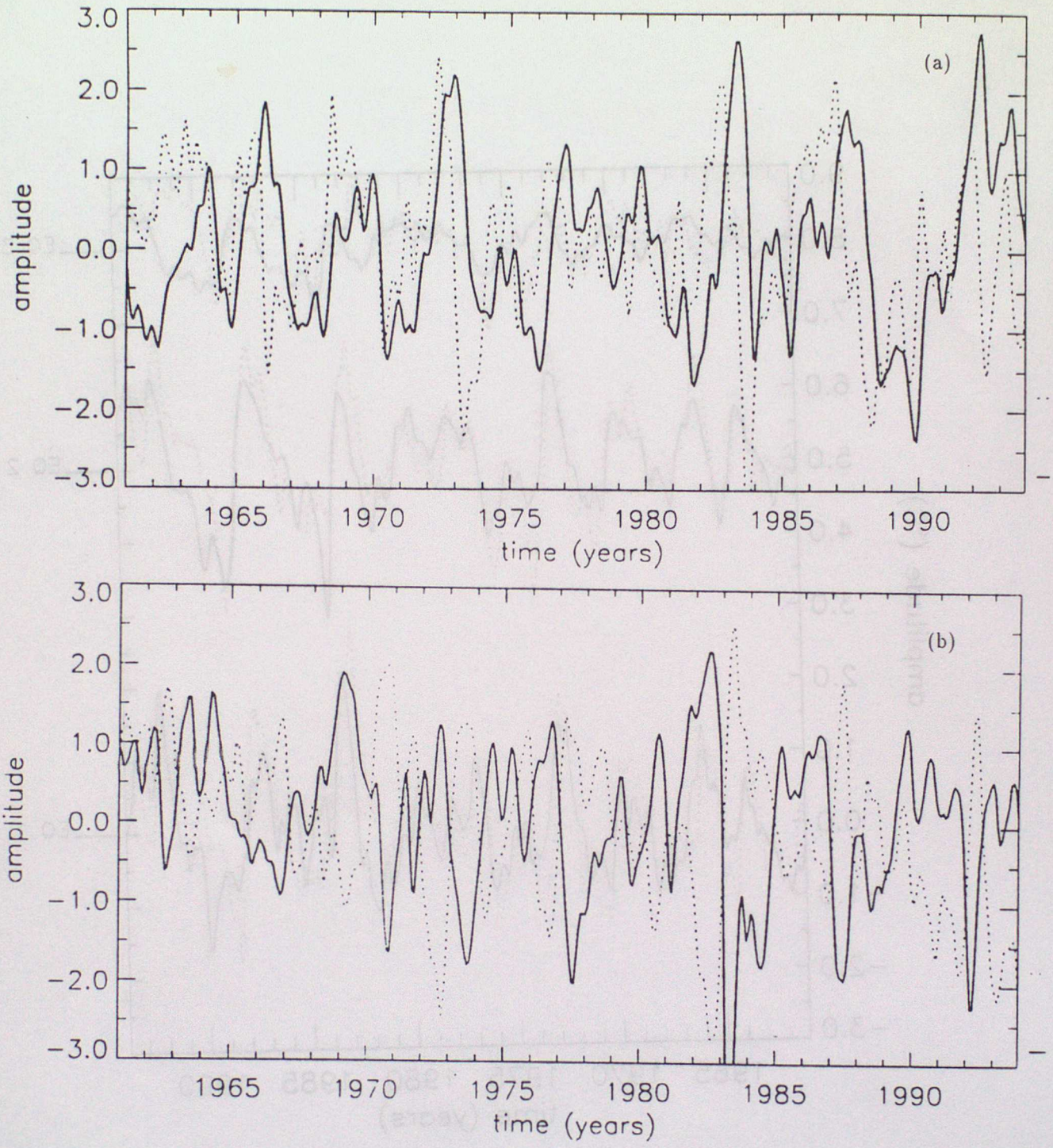

Fig. 12: (a) Model SST anomalies in Niño3 (solid line) and HC anomalies averaged in the equatorial band 5°N-5°S (dotted line). Note that the HC anomalies tend to lead the SST anomalies. (b) HC anomalies in the latitude bands 5°S-15°S (solid line) and 5°N-15°N (dotted line). Note the tendency for northern and southern HC anomalies to have opposite sign.

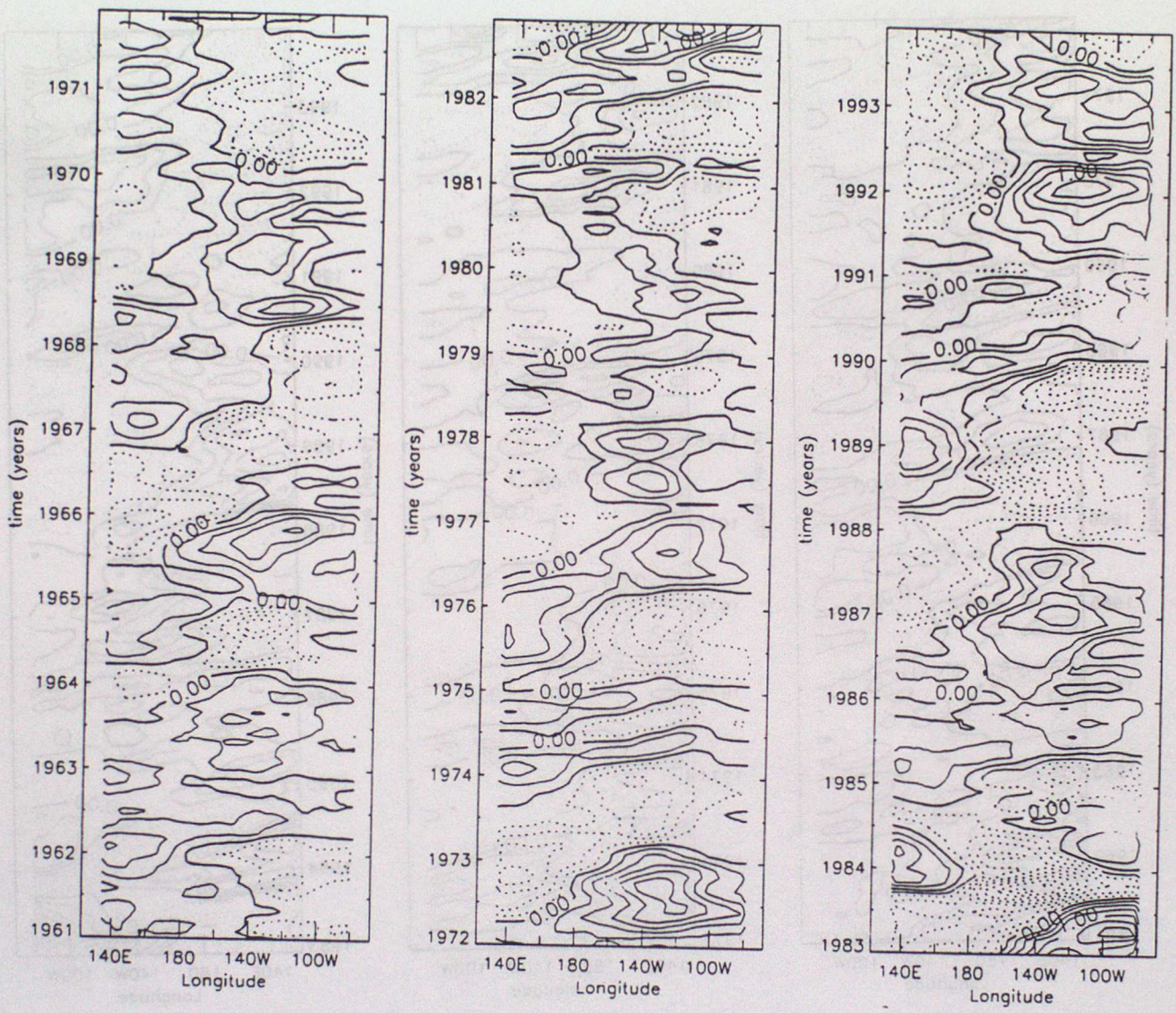

Fig. 13: Time-longitude diagram of equatorial HC anomalies. Negative contours dashed, $ci = 0.25°C$. Note the tendency for eastward propagation, particularly during warm ENSO events.

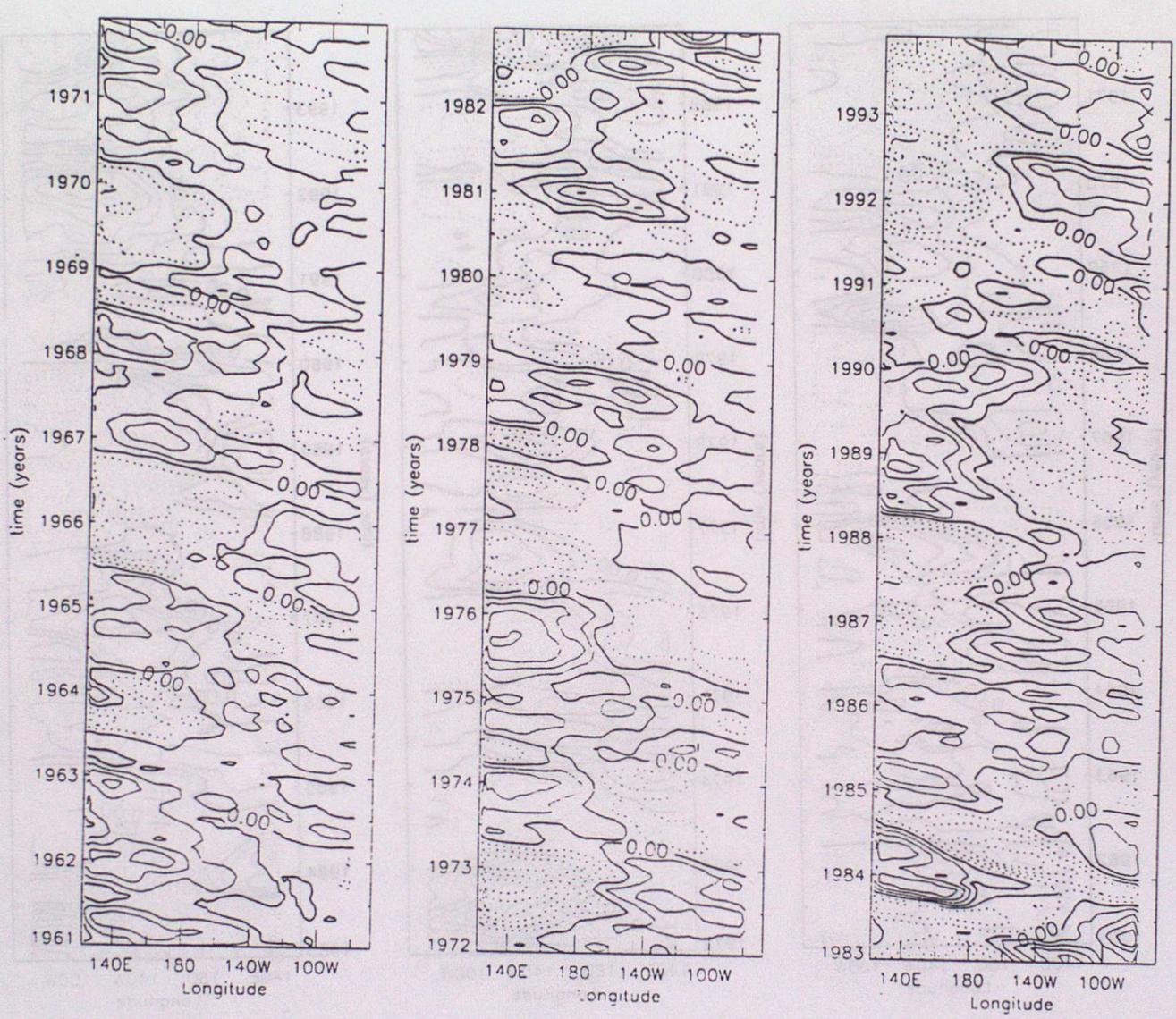

Fig. 14: Time-longitude diagram of the HC anomalies at 5°N. Negative contours dashed, $ci = 0.25$°C. Note the tendency for westward propagation.

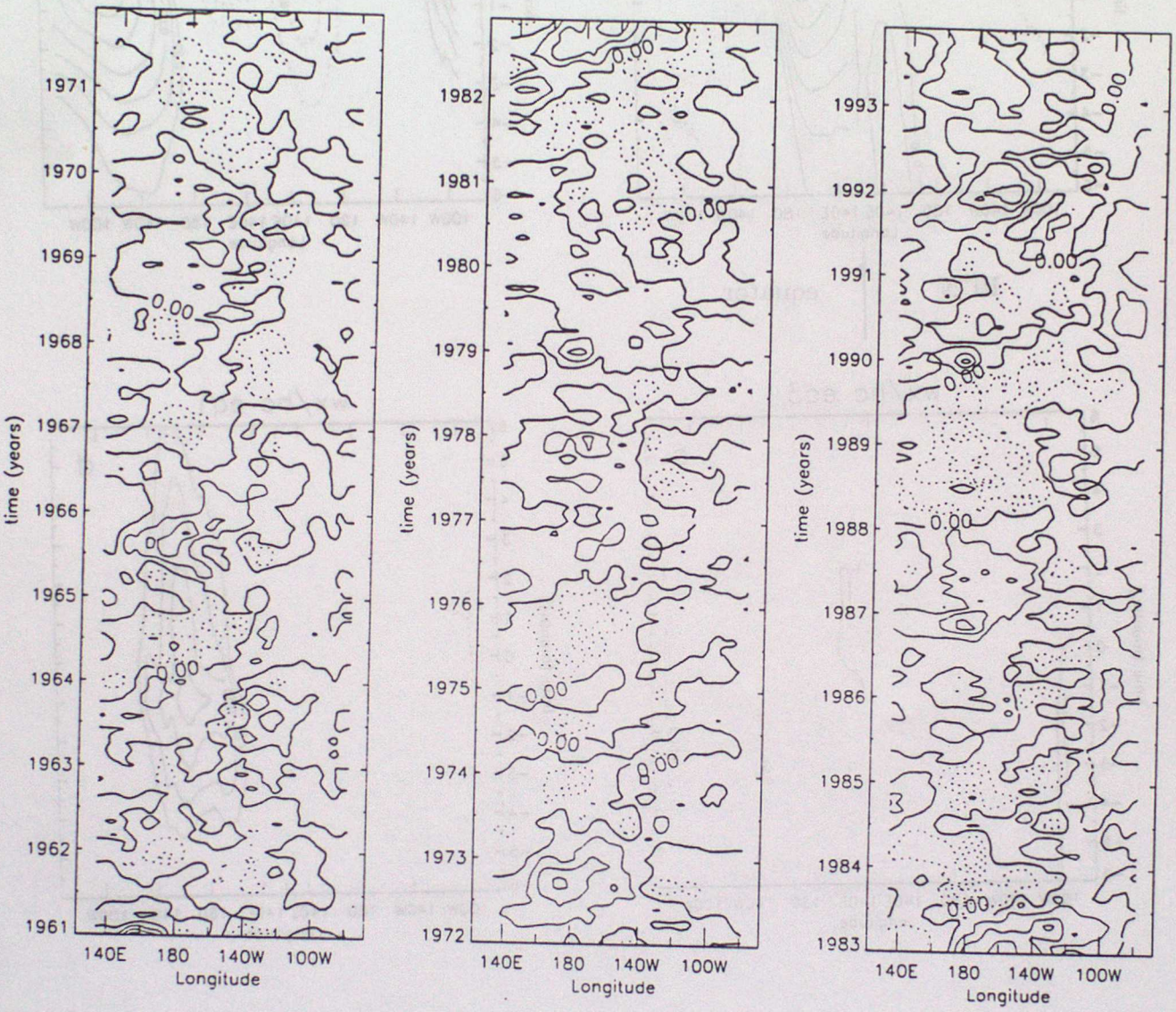

Fig. 15: Time-longitude diagram of equatorial zonal wind stress anomalies. Negative contours dashed, $ci = 0.01$Pa.

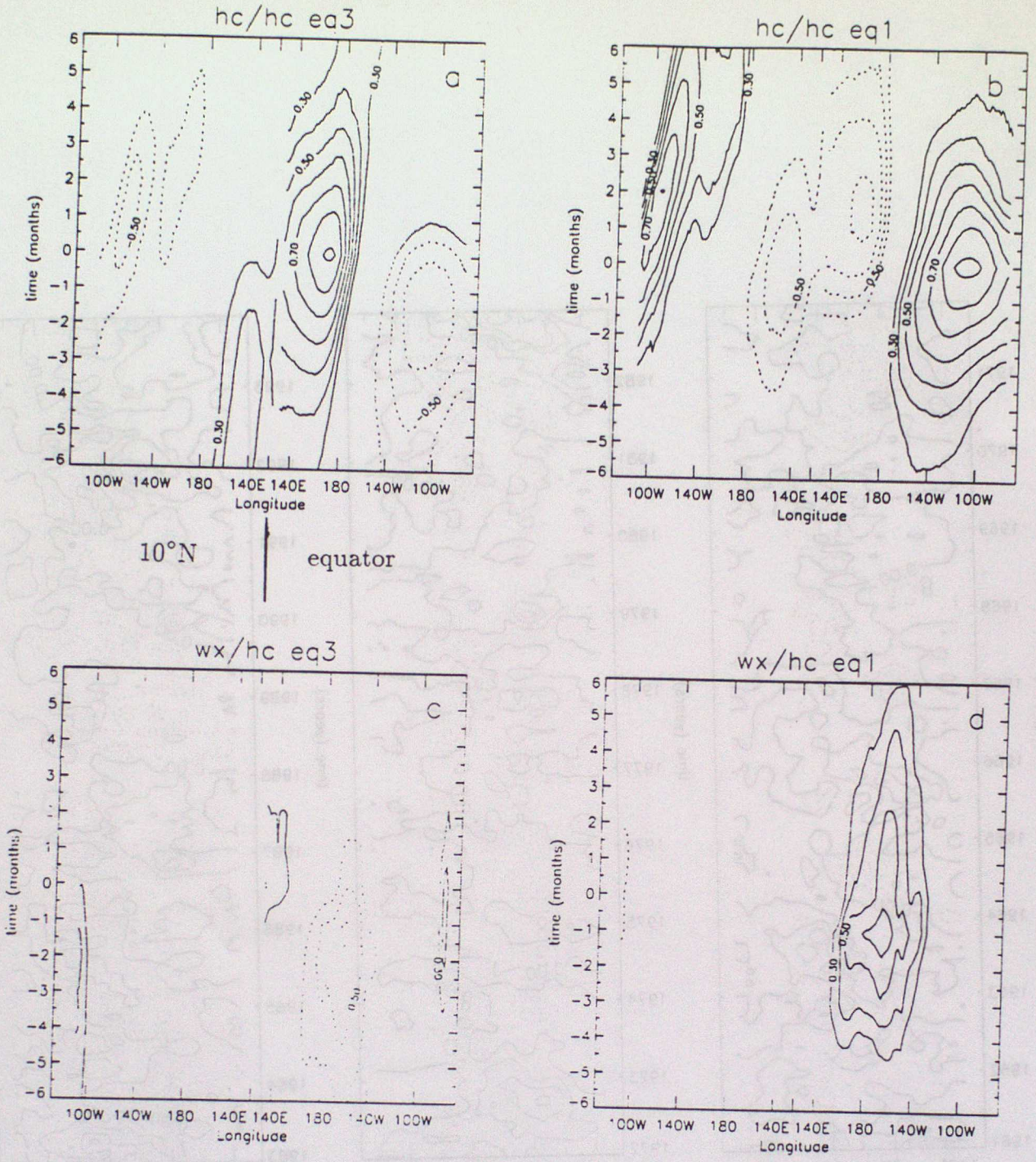

Fig. 16: Heat content and zonal wind stress (τ_x) anomalies at a range of longitudes, correlated for a range of lags with heat content anomalies in regions EQ3 and EQ1. In the left half of each panel, longitude runs from east to west along 10°N: in the right half longitude runs from west to east along the equator. (a) HC anomalies correlated with HC at EQ3 in the west Pacific. (b) HC anomalies correlated with HC at EQ1 in the east Pacific. (c) τ_x anomalies correlated with HC at EQ3 in the west Pacific. (d) τ_x anomalies correlated with HC at EQ1 in the east Pacific. Negative contours dashed, $ci = 0.1$: only contours for correlations ≥ 0.3 or ≤ -0.3 are shown.

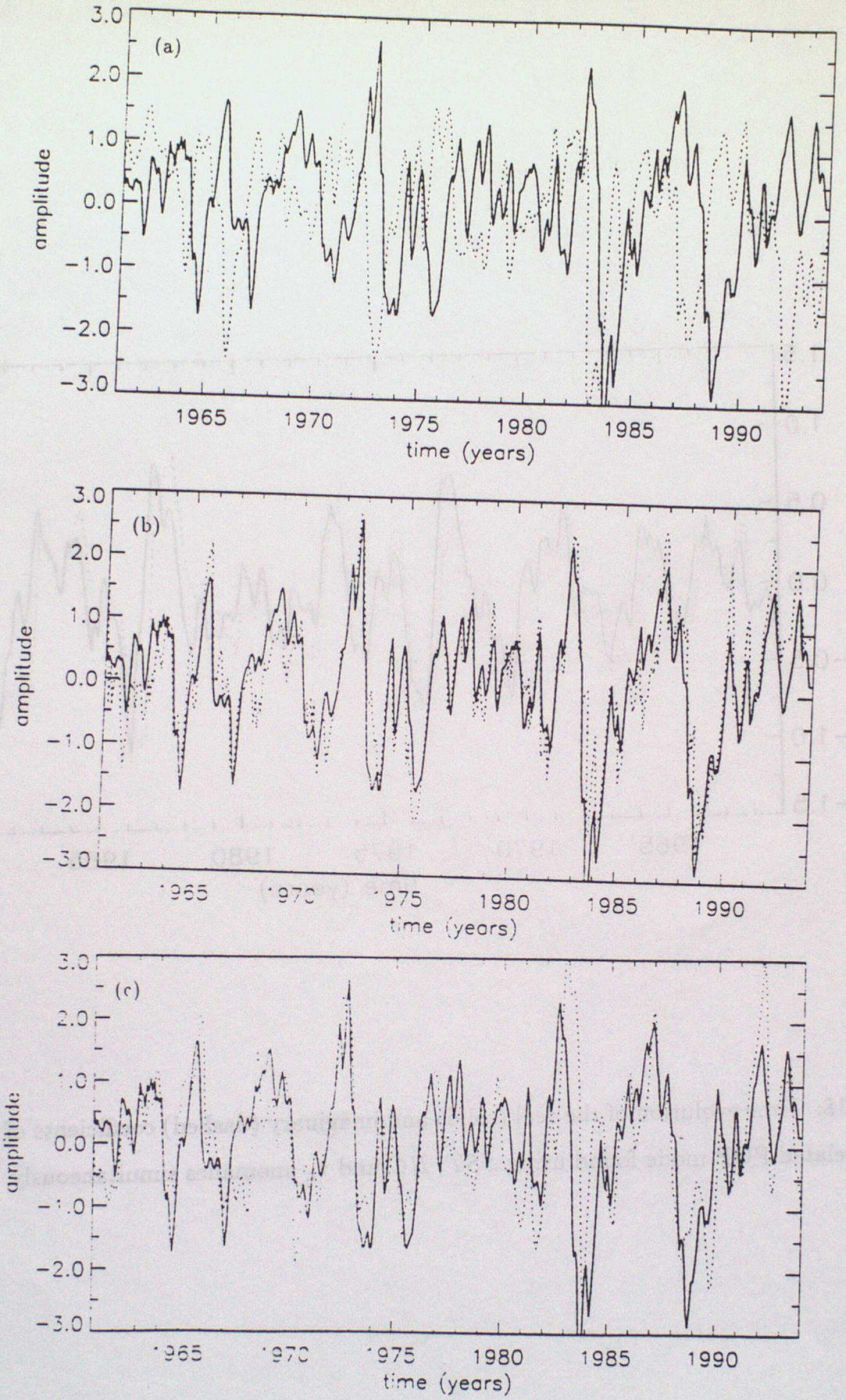

Fig. 17: Time series of HC anomalies in different regions. (a) The anomalies of HC in EQ3 (dotted) and EQ2 (solid) tend to have opposite sign. (b) The anomalies of HC in EQ2 (solid) are highly correlated with the anomalies of τ_x in EQ3 (dotted) to the west. (c) The anomalies of HC in EQ1 (dotted) are related to the anomalies in EQ2 (solid), often with a short lag that suggests wave propagation between the regions.

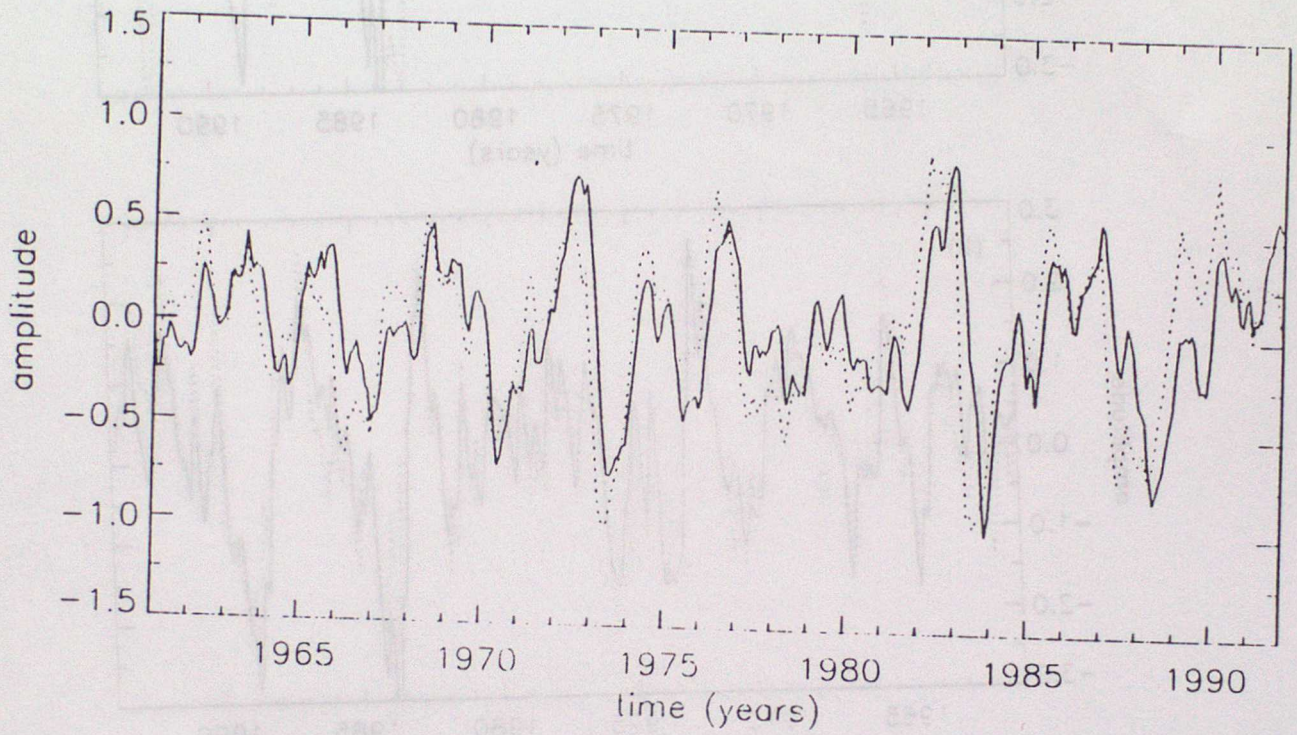

Fig. 18: Time evolution of the real (solid) and imaginary (dashed) coefficients of the ENSO-related POP mode found using SST, HC and τ_x anomalies simultaneously.

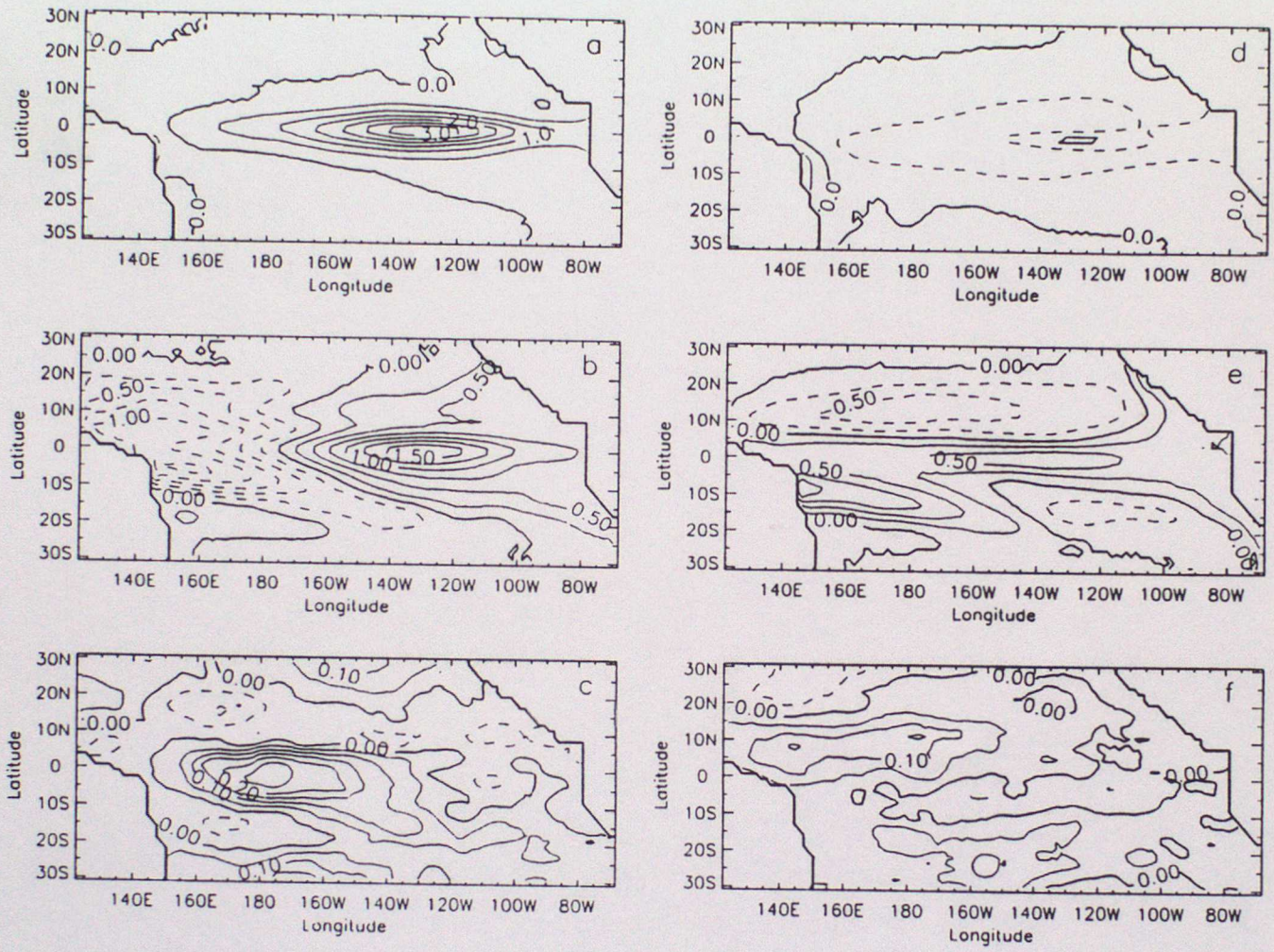

Fig. 19: Spatial patterns of the ENSO-related POP mode. Patterns P (real) are shown on the left, and patterns Q (imaginary) appear on the right. SST anomalies are in panels (a) and (d), HC anomalies are in panels (b) and (e), and τ_x anomalies are in panels (c) and (f).

CLIMATE RESEARCH TECHNICAL NOTES

CRTN 1	Oct 1990	Estimates of the sensitivity of climate to vegetation changes using the Penman-Monteith equation. P R Rowntree
CRTN 2	Oct 1990	An ocean general circulation model of the Indian Ocean for hindcasting studies. D J Carrington
CRTN 3	Oct 1990	Simulation of the tropical diurnal cycle in a climate model. D P Rowell
CRTN 4	Oct 1990	Low frequency variability of the oceans. C K Folland, A Colman, D E Parker and A Bevan
CRTN 5	Dec 1990	A comparison of 11-level General Circulation Model Simulations with observations in the East Sahel. K Maskell
CRTN 6	Dec 1990	Climate Change Prediction. J F B Mitchell and Qing-cun Zeng
CRTN 7	Jan 1991	Deforestation of Amazonia - modelling the effects of albedo change. M F Mylne and P R Rowntree
CRTN 8	Jan 1991	The role of observations in climate prediction and research. D J Carson
CRTN 9	Mar 1991	The greenhouse effect and its likely consequences for climate change. D J Carson
CRTN 10	Apr 1991	Use of wind stresses from operational N.W.P. models to force an O.G.C.M. of the Indian Ocean. D J Carrington
CRTN 11	Jun 1991	A new daily Central England Temperature series, 1772-1991. D E Parker, T P Legg and C K Folland
CRTN 12	Jul 1991	Causes and predictability of Sahel rainfall variability. D P Rowell, C K Folland, K Maskell, J A Owen, M N Ward

CLIMATE RESEARCH TECHNICAL NOTES

CRTN 13	Jul 1991	Modelling changes in climate due to enhanced CO2, the role of atmospheric dynamics, cloud and moisture. C A Senior, J F B Mitchell, H Le Treut and Z-X Li
CRTN 14	Sep 1991	Sea temperature bucket models used to correct historical SST data in the Meteorological Office. C K Folland
CRTN 15	Aug 1991	Modelling climate change, and some potential effects on agriculture in the U.K. P R Rowntree, B A Callander and J Cochrane
CRTN 16	Aug 1991	The Boreal Forests and Climate G Thomas and P R Rowntree
CRTN 17	Aug 1991	Development of a Stratosphere-Troposphere Data Assimilation System. R Swinbank.
CRTN 18	Sep 1991	A study of asynchronous coupling using a simple climate model. M K Davey.
CRTN 19	Sep 1991	The Oceanic Carbon Cycle. N K Taylor
CRTN 20	Nov 1991	Worldwide ocean-atmosphere surface fields in Sahel wet and dry years using provisionally corrected surface wind data. M N Ward
CRTN 21	Dec 1991	Coupled tropical ocean global atmosphere models at the UKMO. M K Davey, C Gordon, S Ineson and S Lawrence
CRTN 22	Dec 1991	Empirical parameterisation of tropical ocean-atmosphere coupling. M Allen, M K Davey, D L T Anderson and P D Killworth
CRTN 23	Feb 1992	The temporal evolution of Equatorial Currents in the Indian Ocean D L T Anderson, D J Carrington, R A Corry and C Gordon
CRTN 24	Feb 1992	Stratospheric analyses provided by the U.K. Meteorological Office M J Bailey, A O'Neill and V D Pope

CLIMATE RESEARCH TECHNICAL NOTES

CRTN 25	Feb 1992	Modelling interannual variability in the Indian Ocean using momentum fluxes from the UKMO and ECMWF operational weather analyses. D L T Anderson and D J Carrington
CRTN 26	Mar 1992	A GCM simulation of the impact of Amazonian deforestation on climate using an improved canopy representation J Lean and P R Rowntree
CRTN 27	Mar 1992	The parameterization of rainfall interception in GCMs A J Dolman and D Gregory
CRTN 28	Jun 1992	Development of worldwide marine data eigenvectors since 1985 A W Colman
CRTN 29	Jun 1992	A tropical ocean model with reduced physics M K Davey
CRTN 30	Jun 1992	International Temperature Workshop, Boulder, Colorado, USA, 16 January 1992 Edited by D E Parker
CRTN 31	Jul 1992	Simulation of clear-sky outgoing longwave radiation over the oceans using operational analyses A Slingo and M J Webb
CRTN 32	Sep 1992	A prediction of the transient response of climate J M Murphy
CRTN 33	Nov 1992	LEPS scores for assessing climate model simulations and long-range forecasts. C K Folland
CRTN 34	Jan 1993	Stratospheric Data Assimilation System Guide Editer: R Swinbank
CRTN 35	Mar 1993	A Stratosphere-Troposphere Data Assimilation System R Swinbank and A O'Neill
CRTN 36	Mar 1993	Validation of hydrological schemes for climate models against catchment data. P R Rowntree and J Lean

CLIMATE RESEARCH TECHNICAL NOTES

CRTN 37	Apr 1993	Modelling of palaeoclimates: Examples from the recent past J F B Mitchell
CRTN 38	May 1993	A simulation of seasonality in ENSO forecast skill M K Davey, D L T Anderson and S Lawrence
CRTN 39	Jul 1993	ENSO Prediction experiments using a simple ocean-atmosphere model D-H Wu, D L T Anderson and M K Davey
CRTN 40	Sep 1993	Diagnosis of dynamic sea-surface and sea-level changes from the Cox ocean model J M Gregory
CRTN 41	Sep 1993	Seasonal variations of the clear-sky greenhouse effect: the role of changes in atmospheric temperatures and humidities M J Webb, A Slingo and G L Stephens
CRTN 42	Nov 1993	Sea-level changes under increasing atmospheric CO_2 in a transient coupled ocean-atmosphere GCM experiment. J M Gregory
CRTN 43	Dec 1993	Global and regional patterns of climate change: recent predictions for the Arctic P R Rowntree
CRTN 44	Feb 1994	The effect of changing horizontal diffusion in the atmospheric version of the unified climate model C D Hall and R A Stratton
CRTN 45	Mar 1994	Simulation of El-Niño/Southern Oscillation like variability in a global AOGCM and its response to CO_2 increase. S F B Tett
CRTN 46	Apr 1994	Global data required for monitoring climate change. D E Parker and C K Folland
CRTN 47	May 1994	Seasonal uptake of anthropogenic CO_2 in an ocean general circulation model. N K Taylor

CLIMATE RESEARCH TECHNICAL NOTES

CRTN 48 Jun 1994 A tropic-wide oscilation of boreal summer rainfall and patterns of sea-surface temperature.
M N Ward, K Maskell, C K Folland, D P Rowell and R Washington

CRTN 49 Jun 1994 Simulation of the tropical Pacific using a simplified ocean model
M A Balmaseda, D L T Anderson and M K Davey